ENHANCED DEPTH AND LOCATION DETERMINATION OF CONDUCTING MARINE MINES

MASOUD MAHMOUDI

School of Electrical and Electronic Engineering

A thesis submitted to the Nanyang Technological University
in fulfillment of the requirement for the degree of
Master of Engineering

2009

Abstract

Marine mines submerged in seawater or buried in beaches are a common danger in many areas of the world. The majority of marine mines are composed of metal and explosive materials. A novel scheme for detecting the location and depth of a metallic mine (modeled as a perfectly conducting sphere and spheroid) in marine environment is presented. This technique takes into account Eddy-Current Response (ECR) induced on the conducting marine mines as well as Current-Channeling Response (CCR) associated with the perturbation of currents induced in the conductive marine environment. It leverages on the unique electromotive force (EMF) induced in a receiving coil through different orientations of a transmitting coil with respect to the marine mine. Unlike conventional electromagnetic (EM) sensing apparatus which is used to carry out the measurement at just one attitude at a fixed angle with respect to buried mine, our proposed scheme consists of angular scanning via the symmetry axes of a concentric sensor over the metallic mine in order to obtain a unique normalized induced voltage determining the mine's depth and location. Simulated results show that this technique has the potential of extending the depth of detection range up to 2 meters away from the sensor as well as enhancing the accuracy of detection in the conductive environment and sea water. The performance is superior to the current method available for the same application.

Acknowledgments

First of all, I would like to thank Dr. TAN Soon Yim, my advisor, who initially proposed me this interesting topic for my thesis, and who has helped me providing the answer of many questions and unclear concepts during every step of such comprehensive research. His kind support as an advisor at the Nanyang Technological University has been a significant part of my studies.

I would also like to acknowledge the financial support of the Nanyang Technological University at the school of Electrical and Electronic Engineering during my studies to complete the Master of Engineering.

I would also like to express my faithful thanks to all of my friends who did support me both mentally and spiritually during my stay in Singapore by creating a cordial environment as if I was living in my hometown.

Last but not least, I am very grateful of my kind parents and brothers who I am forever indebted and I would have been unable to complete my graduate studies without their assistance, patience and love in the all aspects of my life through these very important years of my life.

Table of Contents

List of Figures

Chapter 1. Introduction and Literature Review

1.1 Forward

A considerable amount of unexploded land mines and marine mines over 60 countries threaten the mankind's life [1-6]. To avoid maiming the innocent civilians in the contaminated areas, the eradication of such mines has been investigated by many military organizations and humanitarian agencies around the world while the disposal of marine mines are more arduous and expensive than the same mines embedded in lands [7-12]. Recently what is more laborious is not just to detect the unexploded ordnances, but to identify and discriminate them [13, 14]. Their identification and discrimination would involve determining the depth, location and orientation of buried mines [15-18]. Here were are going to utilize the conventional mine detectors (sensors) in order to determine the location and depth of conducting marine mines.

1.2 Previous works and Existing Sensors

Several detection methods such as Ground Penetrating Radar (GPR), metal detector and Electromagnetic Induction (EMI) sensing have been found to explore and discriminate mines in various environments and determine their depth [19-26].

Electrical Impedance Tomography (EIT) and (GPR) are the two commonly used techniques in this group. EIT uses electrical currents to image the conductivity distribution of the medium under investigation [10, 11]. The technology is appropriate for detecting all types of mines.

Moreover, it is especially well suited for mine detection in wet environments, because of the enhanced conductivity of the moist substrate. The drawback of this technique referring to its low penetration depth is still a big challenge for the detection of conventional marine mines [11].

GPR detects buried objects by emitting waves into the ground and then analyzing the return signals generated by reflections of the waves at the boundaries of materials with different indices of refraction caused by differences in electrical properties [22, 23]. The key point in this method is that the lowest frequencies offer the best penetration, but a wideband technique appears to be necessary in order to get the fine details. It is a well-known method especially for discerning non-metallic landmine in shallow depth based on the dielectric contrast between soil and the mine at the frequency range from 30 MHz to 6 GHz [22]. However it is very sensitive to the soil's moisture, the dielectric contrast between the various intermediate layered medium and the roughness of the surface [23]. The drawbacks of GPR include the large size of its apparatus, its complex operation and its low sensitivity compared to metal detectors [22]. In spite of its penetration depth in dry soil which could be up to 15 m, it has a very low penetration depth of few centimeters in moist soil and marine environments [28, 29]. The Generic algorithm with an EM model fusion in microwave X-band demonstrates the complexity of GPR method proposed to estimate the depth through segmenting a suspected region [16].

The basic metal detector used for mine detection measures the back-scattered portion of an emitted electromagnetic field caused by the reflection of metallic objects inside the mine embedded in the ground [16]. Some detectors create an image of the object being detected instead of producing any audio signal. The currently commercially available detector is able to detect and see metal parts of less than 1cm to a depth of 50cm [7]. The others are magnetic

sensors and measure a magnetic field. Sending a current through a wire wrapped around a metal rod or loop produces a magnetic field that penetrates the ground. The ground disrupts the magnetic field, which is measured by the magnetometer.

Acoustic/seismic methods look for mines by *vibrating* them with sound or seismic waves that are introduced into the ground. Materials with different properties vibrate differently when exposed to sound waves [7]. Nowadays it is not a popular method owing to its considerable defects such as not detecting mines buried deep underground because the resonate response attenuates significantly with depth. In addition, it is also sensitive to heavy vegetation [9].

Electromagnetic Induction Spectroscopy (EMIS) is a relatively new method of classifying a hidden metallic object, such as a landmine, based on its spectral response over a broad induction bandwidth [14]. Most metal detectors can detect small metal pieces but cannot effectively discriminate them from a landmine and false alarms due to clutters in the environment. False alarms are an event caused by other metallic objects, soil moisture and reflections from environment. A major research area is to develop discrimination capabilities [12]. When an electrically conductive and/or magnetically permeable object; i.e., metals, ferrous or nonferrous, is put in a time-varying EM field, a system of induced current flows through the object. Afterwards, a small secondary magnetic field is generated and emanated from the induced current [12, 14]. By observing this secondary field, the object can be detected. The key point in this method is that one can measure the broadband spectrum of the secondary field and then can obtain a distinct spectral signature that may identify the objects. Based on the response spectrum, one can obtain the "fingerprint" of the object. This is the basic concept of EMIS [14].

Recently, many researchers have applied low-frequency EMI sensing to determine the depth and location of a metallic mine with concentric sensors [12, 17, 30-46]. In [39], it was shown that the eigenvalues of magnetic polarizability tensor can be normalised with respect to the depth of the unexploded ordnance (UXO) by applying a multiplicative scale factor at all frequencies. In this method it would be necessary to have access to the library eigenvalues derived from the unknown object after normalizing for the depth. Another method for the depth up to 2 m was suggested on the basis of simplified analysis in which the depth of an object subjected to a pulsed magnetic field can be determined from the ratio of voltages induced in two receiver coils, irrespective of the object‘s size [38]. The induced eddy currents for the conducting spheres are used to validate this method [43, 44].

1.3 Motivations of Thesis

The most common mines found in water are composed of metals and explosive [12]. In fact due to the huge size of common marine mines, using the plastic mine is not applicable and suitable. On the other hand, the small-size non-metallic mines are used for the anti-personal mines to escape detection in lower depths. Actually some so-called “plastic mines” contain a noticeable amount of metal [13, 14]. In the method proposed for the detection of metallic mine’s depth in [38] the nonlinearity of the mine’s depth to the voltage ratio indicates two possible depths, which would be time-consuming to overcome in real-time discrimination. So finding a new technique in order to determine the depth and location of marine mine using the conventional EM sensors, like GEM-3 and GEM-5, which are able to detect small-size metallic mines can be considered as a significant motivation.

1.4 Proposed System and Objectives of Thesis

Most of the conventional electromagnetic sensing apparatus with concentric sensors carry out the measurements at just one altitude at a fixed angle at top of the surface in which the mine is buried [14, 25, and 38]. In this research we are going to find a novel scheme to determine the location and depth of perfectly conducting spherical and spheroidal mines embedded in marine environment through the angular scanning of the transiting and receiving coil.

The conductive background medium is assumed to be homogenous with a uniform conductivity σ_s and the object is illuminated with a time-varying electromagnetic fields emanating from the common suitable concentric sensors for underwater applications, e.g. GEM-3 and GEM-5. The basis of our method is similar to the EMIS in which the broadband spectrum of the secondary magnetic field is used to discriminate the types of mines via the concentric sensors GEM-3 and GEM-5. Here, our scheme relies on the angular scanning of the same coils in order to obtain a unique induced response at any specific depth and location.

Three different configurations of buried spheroidal mines as the representatives of common deployments of marine mines will be discussed.

1.5 Contributions of Thesis

In this research a novel scheme to determine the location and depth of broad-range perfectly conducting spherical and spheroidal mines embedded in marine environment is presented. Through angular scanning we provide a practical approach to measure the Current-Channeling

Response (CCR) especially over the range of depth for which it can exceed the Eddy-Current Response (ECR), thus causing an increment in the detection range in the marine environment up to about 2 meters away from the metallic mine.

The uniqueness of the normalized EMF pertaining to the induced voltage in the concentric sensor through angular scanning with respect to the marine mine demonstrates how one can discern the location of both spherical and spheroidal conducting mines at any specific depth.

1.6 Outlines of Thesis

In chapter 2, we first investigate Maxwell's equations in order to derive the analytical solutions for the electric and magnetic fields generated by the common concentric sensors which are modeled as magnetic dipoles.

In chapter 3, an analysis of the depth-detection technique of spherical mines through separated-coil system is shown. In this chapter we look for the analytical solution for Eddy-Current and Current-Channeling separately by the spherical objects in the weakly conducting background medium, and then we render a new method that causes an enhancement in the analytical solution for finding the effect of Eddy-Current in the weakly conducting background medium.

In chapter 4, at first we compare the backscattered induced EMF response of a spheroid with a sphere of the same radius and then the pertinent derivations for spheroidal mines with unified coils are given in this section.

In chapter 5, the effectiveness of this scheme is presented through numerical results. We will compare our proposed method with the previous one and will show its capability in the background medium with bulk conductivity such as moist soil.

Subsequently, the conclusion is given in chapter 6.

Chapter 2. Electromagnetic Induction Principles

The production of an electrical potential difference in a conductor situated in a changing magnetic flux is considered as the concept of Electromagnetic induction response. In this chapter, we are using Maxwell's equations to derive the theory of induction responses of conducting objects. The electromagnetic induction (EMI) sensor is used to excite the object. The typical sensors such as GEM-3 and GEM-5 consist of coplanar concentric coils denoted as the transmitting and receiving coils. In this chapter, a basic model is considered to demonstrate the induction response. The spherical and spheroidal conducting objects will be investigated which leads to a closed-form solutions of induction response in the concentric receiving coil and the same conclusion regarding the contemporary wide range of landmines and sea mines. These shapes can reveal the essential characteristics of induction response due to any arbitrarily-shaped conducting objects.

Through the use of Maxwell's equations, the problem of electromagnetic induction will be investigated. At the first step the attributes of a simple source are extracted. Using the dipole models which is used to illustrate the loop of current in the sensors, their magnetic and electric fields will be found while the necessary assumptions as will be brought out in the beginning of chapter 3 are applied to simplify the actual problem. After that, the induction response of a solid conducting sphere will be found using the electric and magnetic fields of two-coil EMI system. In fact, the induction response of the sphere and spheroid are derived by applying the electromagnetic boundary conditions at the surface of the sphere and spheroid, separately.

2.1. Implementation of Maxwell's Equation

As shown in Fig. 2.1, our EMI problem involves utilizing a pair of coils to excite and measure the induction response of a buried conducting object. The electromagnetic fields generated by the source coil and also the scattered fields due to the buried object obey the Maxwell's equations [38-46]. The differential form of Maxwell's equations are expressed as follows (the time convention of $\exp(-i\omega t)$ is assumed and suppressed throughout this thesis).

$$\nabla \times \overline{E} = i\omega\mu\overline{H} \tag{2.1}$$

$$\nabla \times \overline{H} = (\sigma - i\omega\varepsilon)\overline{E} + \overline{J} \tag{2.2}$$

where $\overline{H}$ is the magnetic field intensity computed in amps per meter A/m, $\overline{E}$ is the electric field intensity computed in volts per meter V/m and $\overline{J}$ is the electric current density measured in amps per meter squared A/m^2 of any available source.

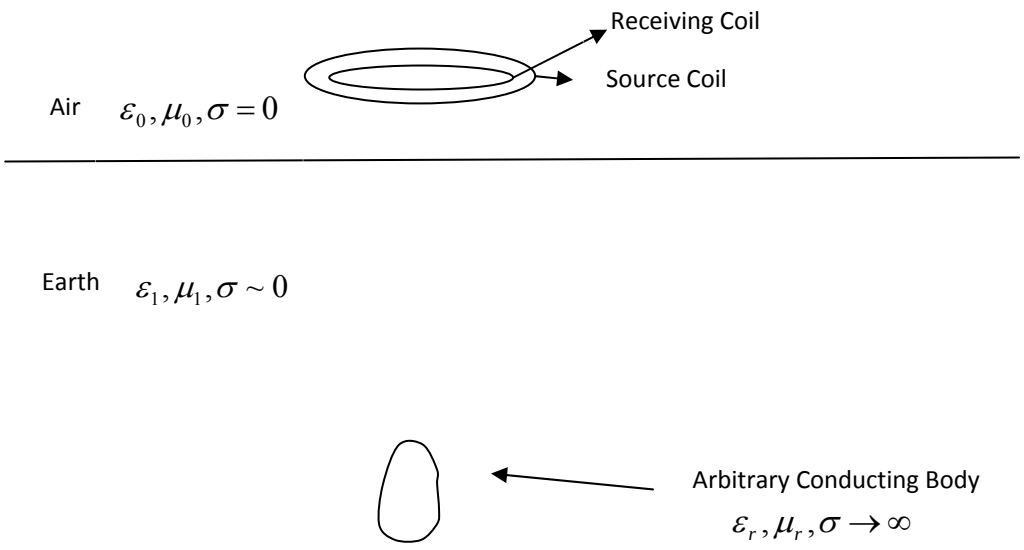

Figure 2-1: Configuration of general EMI system with a buried conducting object

In our problem we use an alternating source to excite the coil, therefore the mentioned electromagnetic fields in our problem have a time dependence which is of the form $\overline{H}(\bar{r},t) = \mathrm{Re}\{\overline{H}(\bar{r},\omega)e^{-i\omega t}\}$, $\overline{E}(\bar{r},t) = \mathrm{Re}\{\overline{E}(\bar{r},\omega)e^{-i\omega t}\}$ and $\overline{J}(\bar{r},t) = \mathrm{Re}\{\overline{J}(\bar{r},\omega)e^{-i\omega t}\}$ where ω is the dominant angular frequency of the exciting source. The Maxwell's equations in our problem are applied to a lossy environment such as sea water or moist soil. The constitutive parameters of lossy environment are: conductivity $\sigma[S/m]$; permittivity $\varepsilon[F/m]$; and permeability $\mu[H/m]$. The assumption of having a homogeneous, linear and isotropic conducting background medium is considered throughout the problem. The divergence of $\overline{H}$ in a linear and isotopic medium is equal to zero. According to this fact that any divergenceless vector can be interpreted as the curl of some other vector, so the magnetic field vector can be shown as

$$\overline{H} = \nabla \times \overline{A} \tag{2.3}$$

where $\overline{A}$ is called the magnetic vector potential. Through the substitution of (2.3) into (2.1) and rewriting the terms, one can find that

$$\nabla \times \left(\overline{E} - i\omega\mu\overline{A}\right) = 0 \tag{2.4}$$

Any curl free vector is mathematically can be expressed as the gradient of some other scalar. Therefore,

$$\overline{E} - i\omega\mu\overline{A} = -\nabla\phi \tag{2.5}$$

where ϕ is the electric scalar potential. By substituting (2.3) and (2.5) into (2.2) and applying the vector derivation, $\nabla \times \nabla \times \overline{A} = \nabla\left(\nabla \cdot \overline{A}\right) - \nabla^2 \overline{A}$, the new equation for $\overline{A}$ is given by

$$\nabla\left(\nabla\cdot\overline{A}\right)-\nabla^2\overline{A}=\left(\sigma-i\omega\varepsilon\right)\left(i\omega\mu\overline{A}-\nabla\phi\right)+\overline{J} \tag{2.6}$$

The divergence and the curl of $\overline{A}$ are independent of each other. For a uniquely defined $\overline{A}$, it is necessary to find both the curl and the divergence of $\overline{A}$ uniquely. To simplify the equation (2.6), the divergence is set as fallows:

$$\nabla\cdot\overline{A}=-\left(\sigma-i\omega\varepsilon\right)\phi \tag{2.7}$$

Therefore the equation (2.6) reduces to

$$\nabla^2\overline{A}+k^2\overline{A}=\overline{J} \tag{2.8}$$

where $k^2=\omega^2\mu\varepsilon+i\omega\mu\sigma$. There are two main advantages for using $\overline{A}$ instead of $\overline{E}$ and $\overline{H}$. The rectangular components of $\overline{A}$ have directly the rectangular components of $\overline{J}$ as the exciting source and there is no constrain on the divergence of $\overline{A}$ to be set zero. There is still no restriction about the media surrounding the conducting object.

2.2. Generated Fields due to a Short Electric Dipole

Here it is assumed an arbitrary current density and then the induced electric and magnetic fields are found through using the magnetic potential $\overline{A}$. Consider a current element or dielectric dipole with length L situated in free space, exciting through a current I. As shown in Fig. 2.2 the current element is in the z-direction and situated at the origin of the coordinate. As the only component of the current is in the z-direction, the magnetic vector $\overline{A}$ has only a z component, and that satisfies

$$\nabla^2 A_z + k^2 A_z = 0 \tag{2.9}$$

every point of the space except the origin. The scalar quantity A_z is spherically symmetric because it has a point source at the origin. Thus, substituting $A_z = A_z(r)$ into (2.9) produces

$$\frac{1}{r^2}\frac{d}{dr}\left(r^2 \frac{dA_z}{dr}\right) + k^2 A_z = 0 \tag{2.10}$$

which A_z has two solutions. Here we choose the solution which the wave traveling outward. So, A_z has the following form

$$A_z = \frac{IL}{4\pi r} e^{+ikr} \tag{2.11}$$

by substituting (2.11) into (2.3), the magnetic field created by the current element is found. Subsequently the electric fields are found by substituting the computed magnetic field into (2.1). All the relevant fields are as follows,

$$E_r = \frac{IL\eta\cos\theta}{\lambda^2} e^{+ikr}\left(\frac{1}{2\pi {r_\lambda}^2} + i\frac{1}{4\pi^2 {r_\lambda}^3}\right)$$

$$E_\theta = \frac{IL\eta\sin\theta}{\lambda^2} e^{+ikr}\left(-i\frac{1}{2r_\lambda} + \frac{1}{4\pi {r_\lambda}^2} + i\frac{1}{8\pi^2 {r_\lambda}^3}\right) \tag{2.12}$$

$$H_\phi = \frac{IL\sin\theta}{\lambda^2} e^{+ikr}\left(-i\frac{1}{2r_\lambda} + \frac{1}{4\pi {r_\lambda}^2}\right)$$

where $r_\lambda = r/\lambda$ and η is the intrinsic impedance of the medium.

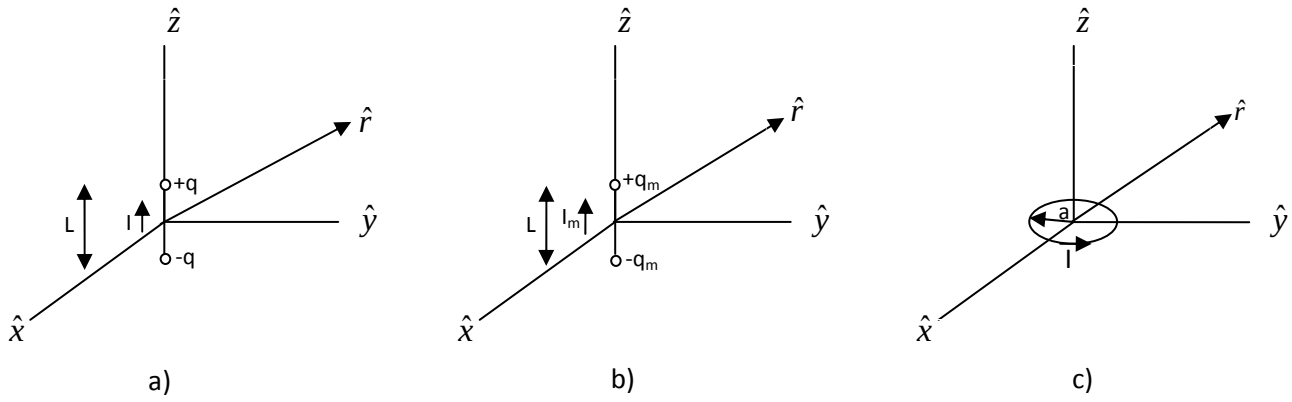

Figure 2-2: a) Small electric current element or electric dipole. b) Short magnetic current element or magnetic dipole. c) Small loop of electric current.

much smaller than the wavelength λ the magnetic and electric fields are computed in the limit as $r_\lambda \to 0$. On the other hand, the continuity equation can relate the current I to the total charge on the current filament as follows

$$q = \int I dt = -I/i\omega \tag{2.13}$$

Using the equation (2.13) and considering the r^{-3} terms which dominate in E_r and E_θ as well as the term r^{-2} which dominates in H_ϕ , one can reduce the electric dipole fields found in (2.12) as follows

$$\begin{aligned} E_r &= -\frac{I}{i\omega}\frac{L}{2\pi\varepsilon\cdot r^3}\cos\theta = \frac{qL}{2\pi\varepsilon\cdot r^3}\cos\theta \\ E_\theta &= -\frac{I}{i\omega}\frac{L}{4\pi\varepsilon\cdot r^3}\sin\theta = \frac{qL}{4\pi\varepsilon\cdot r^3}\sin\theta \\ H_\phi &= \frac{IL}{4\pi\cdot r^2}\sin\theta = -i\omega\frac{qL}{4\pi\cdot r^2}\sin\theta \end{aligned} \tag{2.14}$$

The electric and magnetic fields in (2.14) are exactly similar to those associated with the electrostatics fields computed for the fields of two point charges, $+q$ and $-q$, positioned in a distance L. The above derivations can also be considered as the Biot-Savart equations for the magnetic field of a short element with the length of L carrying a steady current I. The term $e^{-i\omega t}$ is the only difference between the equations in (2.14) and the electrostatic and magnetostatic solutions. As the term $-i\omega t$ tends towards zero in the common frequencies applied to the EMI systems, the solutions are interpreted as quasi-static solutions. It should be noted that the quasi-static solution depends on the distance from the source to the object point. So the boundaries in which the quasi-static solutions are valid should be defined. There is no exact boundary setting apart the quasi-static region, but an estimation of the quantitative boundary can be specified as $r_\lambda < 0.01$ [40].

2.3. Generated Magnetic Fields due to a Loop of Current

We used Maxwell's equations to derive the fields from an electrically short current element called electric dipole. In fact the electric dipole is considered as a source that has low current and high voltage. As found in equation (2.14) the electric fields are the dominant terms within the vicinity of the source due to the $1/r^3$ dependence in the electric fields and just $1/r^2$ in the magnetic field [45, 46]. The real source for the EMI systems is a loop of current such as GEM-3 and GEM-5 that have concentric sensors for their measurements. The typical diameter of common transmitting loop is 20-30 cm in an EMI system. In fact the similarity between an EMI source loop and a small current loop is referring to the length of the loop which is very small relative to a wavelength. In fact, a small current loop is a source that has high current and low

voltage. Against the electric dipole, the near field for a magnetic dipole like a current loop is dominantly magnetic. It is possible to derive the near fields producing by the small current loop from the near fields of the electric dipole. As a matter of fact, the fields of all the small sources such as electric dipole, magnetic dipole, electric current loop and magnetic current loop are related to one another and each of them can be calculated by the other one through using the concept of duality and equivalence. In order to find the fields for a small loop of electric current, the fields of a magnetic dipole should be calculated. It should be noted that magnetic dipole and magnetic currents are merely some concepts which only use for the mathematical developments of the fields of electric charges and electric currents, and no one can find them in the nature. On the other hand the fields of a small current loop and a magnetic dipole are equivalent due to their identical fields. As shown in Fig. 2.2 the fields can be identical when

$$I_m L = -i\omega\mu IS \tag{2.15}$$

So the fields of a small current loop can be found by substituting (2.15) into (2.12) and can be shown as

$$H_r = -\frac{ikIS\cos\theta}{\lambda^2} e^{+ikr}\left(\frac{1}{2\pi r_\lambda{}^2} + i\frac{1}{4\pi^2 r_\lambda{}^3}\right)$$

$$H_\theta = -\frac{ikIS\sin\theta}{\lambda^2} e^{+ikr}\left(-i\frac{1}{2r_\lambda} + \frac{1}{4\pi r_\lambda{}^2} + i\frac{1}{8\pi^2 r_\lambda{}^3}\right) \tag{2.16}$$

$$E_\phi = -\frac{i\omega\mu IS\sin\theta}{\lambda^2} e^{+ikr}\left(i\frac{1}{2r_\lambda} - \frac{1}{4\pi r_\lambda{}^2}\right)$$

The common sensors such as GEM-3 and GEM-5 have concentric coils. So we can replace the term IS by $I\pi a^2$. Hence, the near fields for the current loop can be expressed as follows

$$H_r = \frac{IS}{2\pi r^3}\cos\theta$$

$$H_\theta = \frac{IS}{4\pi r^3}\sin\theta \qquad (2.17)$$

$$E_\phi = \frac{i\omega\mu IS}{4\pi r^2}\sin\theta$$

It is important to be noted that the near field of current loop is mainly magnetic due to the $1/r^3$ dependence in the magnetic fields and merely $1/r^2$ in the electric field. Since the electric field is insignificant compared to the magnetic field in the near field, it is common to compute the EMI response for any conducting object on account of magnetic fields and to ignore the electric field especially in the environment with no significant conductivity.

2.4. Assumptions for EMI Response in Conducting Environments

In order to expedite the calculations of the induction response relating to a common EMI system, the following assumptions are applied to Maxwell's equations.

2.4.1. Displacement Currents

It is common to ignore the displacement currents in a conducting object due to their negligible value compared to the conduction current. The wave number in equation (2.8) can be expressed as

$$k^2 = \omega^2 \mu\varepsilon\left(1 + i\frac{\sigma}{\omega\varepsilon}\right) \tag{2.18}$$

where the term $\frac{\sigma}{\omega\varepsilon}$ represents the loss tangent. The conduction currents dominate the displacement current if the loss tangent is significantly greater than one. In this case the term in the parenthesis is imaginary. The displacement current can dominate the conduction current when the loss tangent is considerably less than one and it exists just in the environment in which the higher frequencies applies to the conducting object. The common conducting objects buried in a battlefield have the constitutive parameters ($\varepsilon = \varepsilon_0$, $\mu = \mu_0$, and σ in the order of 10^7 S/m) [12]. As mentioned earlier, the frequency of operation of typically sensors is less than 100 kHz [38]. If one substitutes these values into (2.18), it can be shown that the loss tangent is equal to 1.8×10^{14} which reveals that the conduction current is dominantly greater than the displacement current. The suppression of displacement current with respect to the conduction current is considered for Maxwell's equation in the environment surrounding the buried conducting object. The typically sea water and sediment in marine environment have the conductivity from 0.01 to $0.04\,S/m$. In this manner, the loss tangent is around 2×10^5 which is still considerably greater than one. It is worth mentioning that permeability does not affect the loss tangent when the displacement currents are omitted. So in highly conducting environment, which is our mission throughout our research, the equation (2.8) becomes

$$\nabla^2 \overline{A} + i\omega\mu\sigma\overline{A} = 0 \tag{2.19}$$

2.4.2. Quasi-static Solutions

Most of the conducting objects investigated as a mine are buried at depths less than two meters. Under this circumstance, the distance between the sensor and the buried object compared to the wavelength is considered in the range of quasi-static region. So the quasi-static assumption in the source-free non-conducting regions for the equation (2.19) may simplify it to

$$\nabla^2 \bar{A} = 0 \tag{2.20}$$

and in non-conducting regions having a known current source, we have

$$\nabla^2 \bar{A} = \bar{J} \tag{2.21}$$

Through the quasi-static assumption, the general solution of equation (2.21) at any points outside to the regions in which electric currents are flowing can be expressed as

$$\bar{A}(\bar{r}) = \frac{1}{4\pi} \iiint_v \frac{\bar{J}(\bar{r}_0)}{|\bar{r} - \bar{r}_0|} d^3 r_0 \tag{2.22}$$

where $\bar{r}_0$ depicts the source point, $\bar{r}$ shows the observation point and $d^3 r_0$ refers to differential volumes. It is worth considering that the e^{+ikr} term which appears in the solution of $\bar{A}(\bar{r})$ is neglected due to insignificant value of the distance from the source to the object relative to the wavelength.

2.5. Eddy-Current and Current-Channeling Response in EMI systems

As shown in Fig. 2.3, there are two contributions to the EMI response from a conducting or non-conducting object embedded in a conducting background medium. The first is due to the eddy currents that induce in the object itself, and the second is due to the perturbation of the conduction currents flowing in the background medium when they encounter the object [41]. The idea of using Eddy-Current for finding the response of an object in the conducting background medium was published by Bond et al. in 1991 [44]. In the *limiting* case of a conducting object embedded in a non-conducting medium, the response is due solely to the eddy current while the response of that conducting object in a conducting medium is merely due to the current channeling.

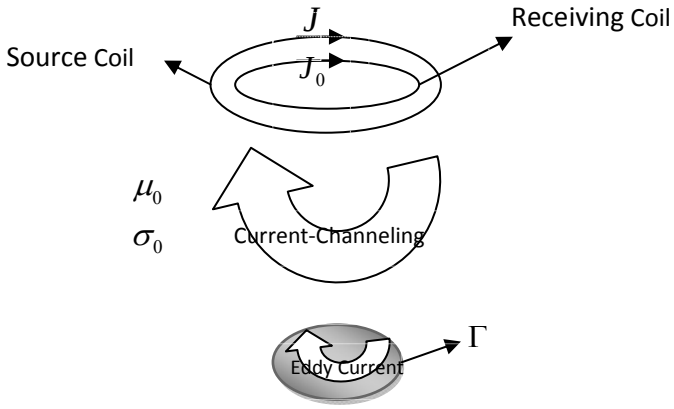

Figure 2-3: Illustration of Eddy-Current and Current-Channeling response in a conducting background environment

In this project, we will extend the above mentioned methods by eddy current and current channeling responses simultaneously for the spherical and spheroidal objects embedded in a conducting background medium. In fact, analyzing the incident and scattered waves from any arbitrary shapes requires a complicated mathematical analysis which cannot satisfy our demands in a closed form formula and on the other hand the results are similar when we have some

assumptions such as being far enough from the object or the dimension of object is smaller than the wavelength [41].

2.6 Conclusion

In this chapter, we investigated the electromagnetic induction process for a typical EMI system. Maxwell's equations are used to the general problem of an arbitrary conducting body illuminated by a current source. Applying the low frequencies and other assumptions, the solution to Maxwell's equations are simplified. Negligible displacement currents compared to conduction currents, elimination of air-earth interface, and quasi static excitation were the simplifying assumption. These assumptions can facilitate the calculation of source field. The results show that the induction response is only dependent on the magnetic fields derived by the Maxwell's equations.

Eddy-Current and Current-Channeling responses are introduced as the two main contributions to the EMI response from a conducting or non-conducting object immersed in a conducting background

Chapter 3. Location Determination of a Conducting Spherical Mine through Separated Transmitting and Receiving Coil

A sphere is often used as a tractable model of a conducting object embedded in a background medium in studying the response of electromagnetic induction (EMI) systems and a spheroid is useful for modeling a much wider range of objects. Prolate and oblate spheroids are useful for modeling ordnance or mines (such as landmines or sea mines). There are two contributions to the EM response of a spherical metal object buried in a conductive medium: from the eddy currents induced in the object and from the current channeling effects within the surrounding medium. An analysis for a sphere having an arbitrary conductivity is complex because the general solution must be expressed as an infinite series of Legendre functions [41]. In [12], the authors derived a closed form formula for a conducting object embedded in a weakly conducting and non-conducting background medium. The geometry of the problem is shown in Fig. 3.1.

Consider an object of finite size, defined by a surface Γ, with conductivity $\sigma(r)$ and permeability $\mu(r)$ embedded in a host medium with conductivity σ_0 and permeability μ_0.

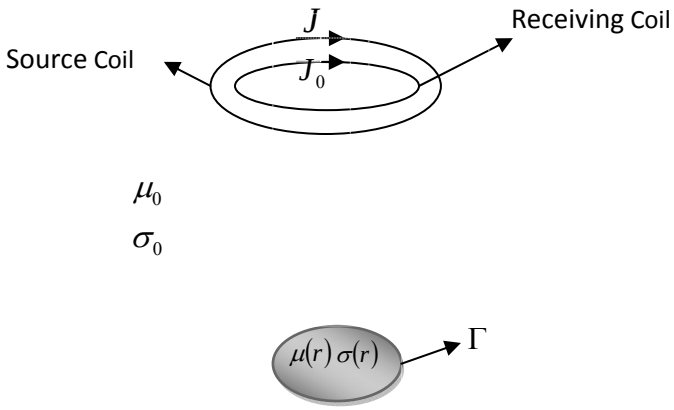

Figure 3-1: The General Geometry for a marine mine detection

A current source generates a known current density $\overline{J}$, located outside the object. The current $\overline{J}$ produces magnetic and electric fields $\overline{H}$ and $\overline{E}$, which obey the Maxwell's equations,

$$\nabla \times \overline{E} = i\omega\mu(r)\overline{H} \tag{3.1}$$

$$\nabla \times \overline{H} = \sigma(r)\overline{E} + \overline{J} \tag{3.2}$$

In addition to the source coil, there is same location as the receiving coil, too. Now, assume the source coil has been turned off $(J = 0)$ and we drive the receiving coil with a hypothetical current density J_0 in the absence of the object and only the presence of the host medium. The resultant fields, H_0 and E_0, generated by J_0 obey the equations,

$$\nabla \times \overline{E}_0 = i\omega\mu_0 \overline{H}_0 \tag{3.3}$$

$$\nabla \times \overline{H}_0 = \sigma_0 \overline{E}_0 + \overline{J}_0 \tag{3.4}$$

If we drive the source coil with the current I, then V shows the open circuit voltage induced in the receiving coil in the presence of the object. Let V_0 express the open circuit voltage induced in the source coil when the hypothetical current I flows in the receiving coil in the absence of the object. Then, from reciprocity principles, the following relation can be derived,

$$V - V_0 = -\frac{1}{I}\int_{\Gamma}\left(\overline{E} \times \overline{H}_0 - \overline{E}_0 \times \overline{H}\right)\hat{n}\, ds \tag{3.5}$$

where $\hat{n}$ is a unit vector perpendicular to Γ. Equation (3.5) can be rewritten as:

$$V - V_0 = -\frac{1}{I}\int_{\Gamma}\left\{\overline{H}_0.\left(n\times\overline{E}\right)+\overline{E}_0.\left(n\times\overline{H}\right)\right\}ds \tag{3.6}$$

Note that, for a perfectly conducting object, the tangential component of the electric field on the surface, $\hat{n}\times E$, vanishes and Equation (3.6) reduces to

$$V - V_0 = -\frac{1}{I}\int_{\Gamma}\overline{E}_0.\left(n\times\overline{H}\right)ds = -\frac{1}{I}\int\overline{E_0}.\overline{K}ds \tag{3.7}$$

where

$$\overline{K} = \hat{n}\times\overline{H} \tag{3.8}$$

$\overline{K}$ is the surface current on the object. All that has been found here is just a general integration formula for finding the electrical potential which has been scattered by some conducting object with arbitrary geometry embedded in a homogeneous background medium. In fact, equation (3.7) is independent of the object geometry or its orientation. But finding the analytical solution for $\overline{K}$ and $\overline{E_0}$ is not always easy for any arbitrary geometries. Therefore, this problem has been solved analytically for spherical and spheroidal objects as the most popular geometries. In fact, to drive a simplifying and closed form formula, we are defining the problem as follows.

Consider a perfectly electric conducting (PEC) sphere as a marine mine embedded in seawater having a uniform conductivity, permeability and permittivity $(\sigma_s, \mu_s, \varepsilon_s)$ as shown in Fig. 3.2. The transmitting and receiving coils are positioned at the distances of d_t and d_r, from the spherical conducting mine of radius a_0, respectively. As depicted, θ_T and θ_R are the angles by which the sphere is displaced from the symmetry dipole axes of the transmitting and receiving

coils, respectively. The following assumptions are made to simplify the derivation of EMF induced in the receiving coil:

1– The transmitting and receiving coils can be approximated as magnetic dipoles having moments $M_T = N_T A_T I_T$ and $M_R = N_R A_R I_R$, where I_T and I_R are the current in the transmitting and receiving coils, while N_T, N_R, A_T and A_R are the number of turns and the effective areas of transmitting and receiving coils, respectively.

2 – The incident fields H_r^i, H_θ^i and E_ϕ^i emanating from the transmitting coil are uniform over the extent of the object. This assumption is valid as in most cases d_t and $d_r >> a_0$.

3 – Sea water is a good conducting medium in such low-frequency range. Thus, displacement current can be neglected. The effect of noise due to the background medium can also be neglected.

On the other hand, for finding eddy current response it is supposed that only the currents induced in the conducting object contribute to the scattered magnetic field i.e., the currents in background medium are neglected, therefore $\sigma_0 \overline{E_0}$ in equation (3.4) is omitted. Similarly for finding current-channeling response, we will only consider the current in the background medium, $\sigma_0 \overline{E_0}$, and neglect the eddy current induced on the surface of the object i.e. the term $i\omega\mu_0 \overline{H}_0$ will be omitted in (3.3).

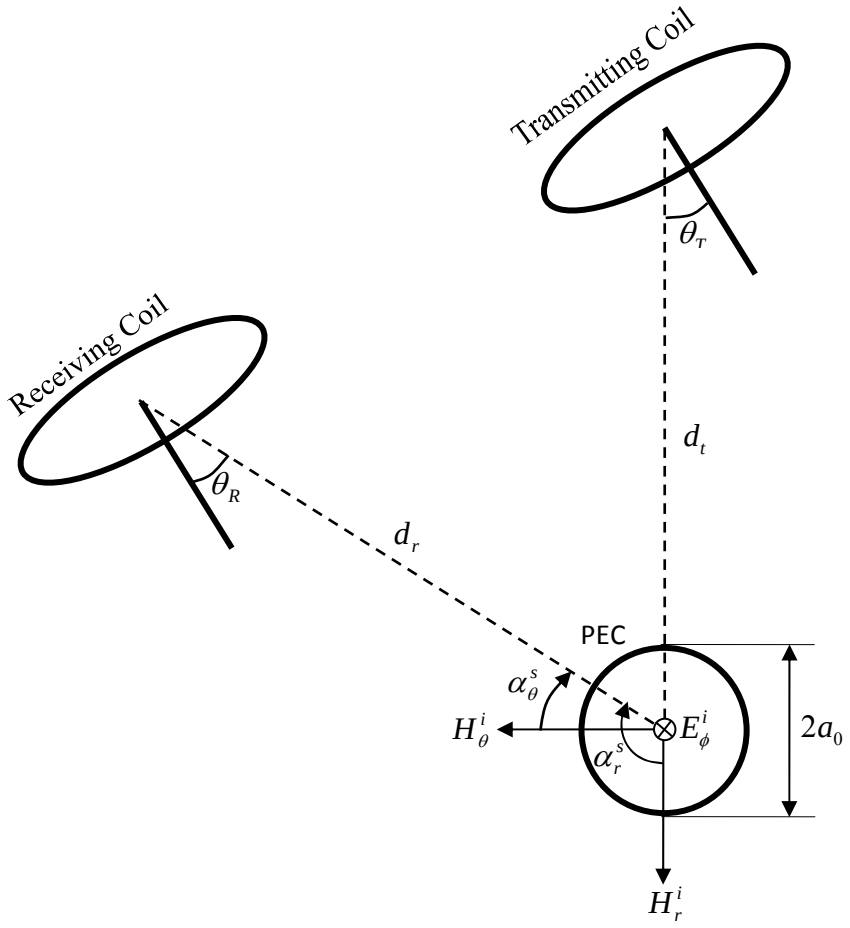

Figure 3-2: General configuration of mine detection through separate transmitting and receiving coils

As shown in Fig. 3.2, the incident fields $\left(H_r^i, H_\theta^i, E_\phi^i\right)$ are given by [41]

$$\overline{H}^i\left(r_t,\theta_t\right)=\hat{r}_t\,H_r^i+\hat{\theta}_t\,H_\theta^i=\frac{M_T}{4\pi r_t^3}\left(2\,\hat{r}_t\cos\theta_t+\hat{\theta}_t\sin\theta_t\right) \tag{3.9a}$$

$$\overline{E}^i\left(r_t,\theta_t\right)=\hat{\phi}_t\,E_\phi^i=\hat{\phi}_t\,\frac{i\omega\mu_s M_T}{4\pi r_t^2}\sin\theta_t \tag{3.9b}$$

where $\hat{r}_t,\hat{\theta}_t$ and $\hat{\phi}_t$ are the unit vectors of spherical coordinates defined with the origin at the centre of the transmitting coil and the zenith angle is measured from its surface normal. At the

location of the object these electric and magnetic fields are equal to $\overline{H}^{i}\left(r_t = d_t, \theta_t = \theta_T\right)$ and $\overline{E}^{i}\left(r_t = d_t, \theta_t = \theta_T\right)$.

There are two contributions to the EMF (induced voltage) in the receiving coil, namely the Eddy-Current and Current-Channeling response [25, 41].

3.1.Eddy-Current Response for a Conducting Sphere

For ECR, the current induced in the metallic mine due to the time varying magnetic field is taken into account. The relevant Maxwell's equations can be written as

$$\nabla \times \left(\overline{H}^{i} + \overline{H}^{s}\right) = 0 \quad , \quad \nabla \cdot \left(\overline{H}^{i} + \overline{H}^{s}\right) = 0 \ , \ \nabla \times \left(\overline{E}^{i} + \overline{E}^{s}\right) = i\omega\mu_s \left(\overline{H}^{i} + \overline{H}^{s}\right) \tag{3.10}$$

By applying the boundary condition of zero normal component of the magnetic field to the surface of the sphere for each term of the incident magnetic field, separately, we can find the total scattered field by

$$\overline{H}^{s}_{EC} = \overline{H}^{s}\left(r_s, \alpha^{s}_{r,\theta}\right) = \overline{H}^{s}_{r}\left(r_s, \alpha^{s}_{r}\right) + \overline{H}^{s}_{\theta}\left(r_s, \alpha^{s}_{\theta}\right) \tag{3.11}$$

$$\overline{H}^{s}_{r}\left(r_s, \alpha^{s}_{r}\right) = \hat{r}_s H^{s}_{r1} + \hat{\alpha}^{s}_{r} H^{s}_{\theta 1} = -\frac{M_T a_0{}^3}{4\pi d_t{}^3 r_s{}^3} \cos\theta_T \left(2\hat{r}_s \cos\alpha^{s}_{r} + \hat{\alpha}^{s}_{r} \sin\alpha^{s}_{r}\right) \tag{3.12a}$$

$$\overline{H}^{s}_{\theta}\left(r_s, \alpha^{s}_{\theta}\right) = \hat{r}_s H^{s}_{r2} + \hat{\alpha}^{s}_{\theta} H^{s}_{\theta 2} = -\frac{M_T a_0{}^3}{8\pi d_t{}^3 r_s{}^3} \sin\theta_T \left(2\hat{r}_s \cos\alpha^{s}_{\theta} + \hat{\alpha}^{s}_{\theta} \sin\alpha^{s}_{\theta}\right) \tag{3.12b}$$

where $\overline{H}^{s}_{r}$ and $\overline{H}^{s}_{\theta}$ are scattered fields due to the incident fields H^{i}_{r} and H^{i}_{θ}, respectively.

In equations (3.12a) and (3.12b), the zenith angles α_r^s and α_θ^s are measured from the direction of incident fields H_r^i and H_θ^i at the origin of PEC, respectively. The induced voltage due to the ECR for a receiving coil with moment M_R and current I_R is given by [37]

$$V_{EC}^{sph} = i\omega \frac{M_R}{I_R} \mu_s \overline{H}_{EC}^s . \hat{n} \tag{3.13}$$

where $\hat{n}$ is the unit vector normal to the receiving coil. The induced voltage due to ECR in the receiving coil shown in Fig. 3.2 is obtained by

$$V_{EC}^{sph}(r_s = d_r, \theta_r = \theta_R) = i \frac{N_T N_R A_R A_T I_T a_0^{\,3}}{2\pi} \frac{\omega \mu_s}{d_t^{\,3} d_r^{\,3}} (\cos\theta_T \cos\theta_R \cos\alpha_r^s + \frac{1}{2}\cos\theta_T \sin\theta_R \sin\alpha_r^s + \frac{1}{2}\sin\theta_T \cos\theta_R \cos\alpha_\theta^s + \frac{1}{4}\sin\theta_T \sin\theta_R \sin\alpha_\theta^s) \tag{3.14}$$

3.2. Current-Channeling Response for a Conducting Sphere

As shown in Fig. 2.3, for CCR, the perturbation of current induced in the sea water (outside of the PEC) is taken into account. The fields obey:

$$\nabla \times \left(\overline{E}^i + \overline{E}^s\right) = 0 \quad , \quad \nabla \cdot \left(\overline{E}^i + \overline{E}^s\right) = 0 \quad , \quad \nabla \times \overline{\widetilde{H}}^s = \sigma_s \overline{E}^s \tag{3.15}$$

where $\overline{E}^i$ and $\overline{E}^s$ are the incident and scattered electric fields, respectively. The scattered electric field, $\overline{E}^s$, must have an associated magnetic field defined by $\overline{\widetilde{H}}^s$. By applying the boundary condition of zero tangential component of the electric field on the surface of the sphere, one can obtain the scattered electric field by

$$\overline{E}^{s}\left(r_s,\alpha_\phi^s\right)=\hat{r}_s\,E_r^s+\hat{\alpha}_\phi^s\,E_\theta^s=\frac{i\omega\mu_s M_T {a_0}^3}{4\pi {d_t}^2 {r_s}^3}\sin\theta_T\left(2\hat{r}_s\cos\alpha_\phi^s+\hat{\alpha}_\phi^s\sin\alpha_\phi^s\right) \tag{3.16a}$$

The corresponding scattered magnetic field can be obtained using (3.15).

$$\overline{H}_{CC}^{s}=\overline{\widetilde{H}}^{s}(r_s,\alpha_\phi^s)=\hat{\phi}_s\,\widetilde{H}_\phi^s=\hat{\phi}_s\frac{i\omega\mu_s M_T\sigma_s {a_0}^3}{4\pi {d_t}^2 {r_s}^2}\sin\theta_T\sin\alpha_\phi^s \tag{3.16b}$$

Thus, the induced voltage due to CCR in the receiving coil with moment M_R and current I_R is

$$V_{CC}^{sph}\left(r_s=d_r,\theta_r=\theta_R\right)=i\omega\frac{M_R}{I_R}\mu_s\overline{H}_{CC}^{s}.\hat{n}=\frac{N_T N_R A_R A_T I_T {a_0}^3}{2\pi}\frac{\sigma_s\omega^2{\mu_s}^2}{2{d_t}^2{d_r}^2}\sin\theta_T\sin\alpha_\phi^s\sin\theta \tag{3.17}$$

where α_ϕ^s and ϕ_s are the zenith and azimuth angles measured by the direction of incident field E_ϕ^i at the origin of PEC, respectively. The total EMF or induced voltage in the receiving coil is equal to

$$V_{tot}^{sph}\left(\alpha_r^s,\alpha_\theta^s,\alpha_\phi^s,\theta_R,\theta_T\right)=V_{EC}^{sph}\left(\alpha_r^s,\alpha_\theta^s,\theta_R,\theta_T\right)+V_{CC}^{sph}\left(\alpha_\phi^s,\theta_R,\theta_T\right) \tag{3.18}$$

where α_r^s, α_θ^s and α_ϕ^s are determined by the relative configuration of transmitting and receiving coils with respect to each other. On the other hand, θ_T and θ_R are merely dependent upon the position of symmetry axes of transmitting and receiving coils with regards to the conducting object.

3.3. Comparison of CCR and ECR for at Different Depths

ECR and CCR variations in different depths could be another hint for assuring this measurement. As depicted in Fig. 3.3 for the depth higher than 4m the CCR is the dominant term which is approximately 10 times higher than ECR and for the depths lower than 2m is vise-versa. Fig. 3.3 verifies that at the depths which ECR is the dominant term, we have merely a partial fluctuation on the total potential through rotating the coils e.g. from 30 to 80 degrees. But for the CCR domination this rotation would result in a considerable increase in the total potential.

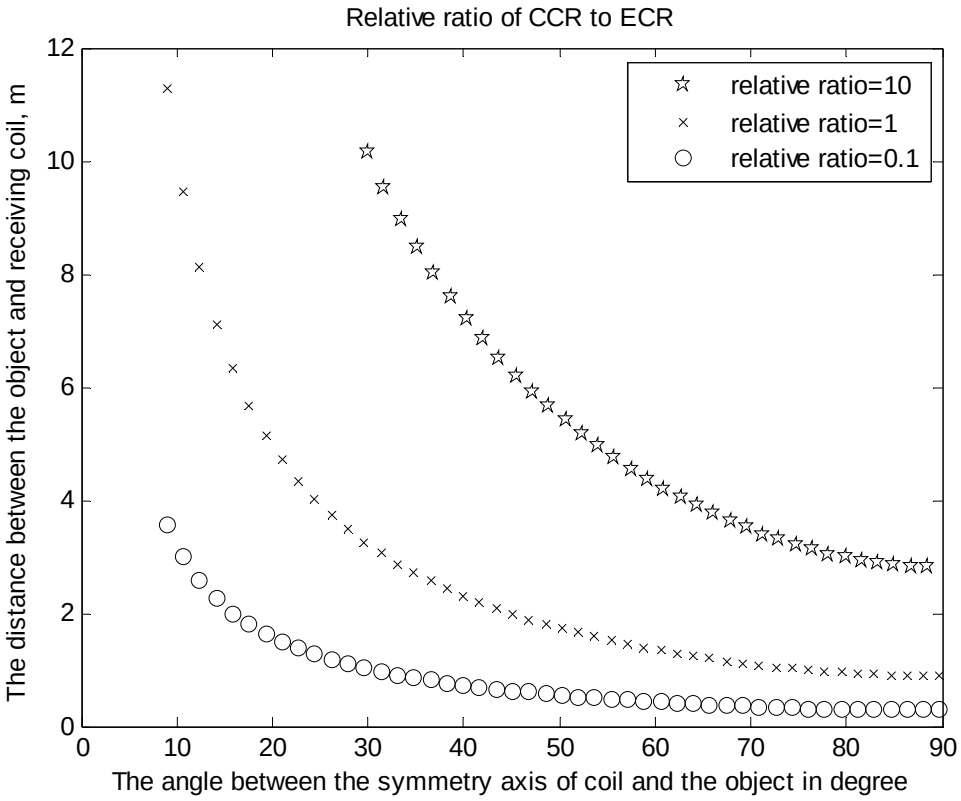

Figure 3-3: Relative ratio of CCR to ECR at different depths for a spherical conducting object

The existence of Current-Channeling response is dependent upon the conductivity of surrounding medium as well as depth of conducting mine. So, ECR and CCR are determined by the conductivity of surrounding medium and depth of mine.

3.4 Conclusion

In this chapter we used sphere and spheroid as the best tractable models in order to represent the broad range of conducting marine mines. Using the surface current on the conducting object we derived the closed form solution for the total induced voltage in the receiving coil. We assumed that that transmitting and receiving coils can be considered as magnetic dipoles and the incident magnetic fields are uniform over the extent of the object. One of the main contributions of this chapter is elaborating detection mechanism by means of separated transmitting and receiving coils. We extracted the induced voltage in the receiving coil for an arbitrary spherical conducting object due to CCR and ECR separately while the deviation angles θ_R and θ_T play a significant role on the induced voltage in the receiving coil. This effect had been suppressed in the previous works [30, 35,37 and 38] and we will demonstrate that how we can take advantage of this feature in order to discriminate the depth and location of conducting marine mine in the next chapters.

Chapter 4. Concentric-Coil System for Spheroidal Conducting Object

In the previous chapters we modeled our conducting marine mine using an arbitrary spherical geometry, then the effect of CCR and ECR were calculated separately and after that we investigated the total induced voltage due to both currents. We demonstrated that how dominantly the deviation angle from the symmetry axis of the transmitting coil can make a significant effect on the total induced voltage in the receiving coil. In the next chapters we explain that how we can find the CCR and ECR for a spheroidal conducting object through the comparison of induced voltages in the transmitting coil with respect to the equivalent spherical conducting object. This achievement makes us capable to expand our detection scheme to a broad range of conducting marine mines.

The behaviors of scattered fields due to a perfectly conducting prolate spheroidal object, as shown in Fig. 4.1, are investigated. In this chapter the major axis of the prolate spheroid is along the z axis while the lengths of the semi minor and semi major axes are a and b, respectively (with $a > b$). In the prolate spheroidal coordinates (ϑ, ξ, ϕ) by setting $\xi = \xi_0 = \text{constant}$, the surface of a specific spheroid can be defined uniquely in which the length of common interfocal distance, 2D, is related to the other parameters in the Cartesian coordinates as follows [47-51]

$$\xi_0 = \frac{a}{D} = \frac{a}{\sqrt{a^2 - b^2}} \tag{4.1a}$$

$$x = D\sqrt{\xi^2 - 1}\sin\vartheta\cos\phi \tag{4.1b}$$

$$y = D\sqrt{\xi^2 - 1}\sin\vartheta\sin\phi \tag{4.1c}$$

$$z = D\xi\cos\vartheta \tag{4.1d}$$

where $1 \le \xi < \infty$, $0 \le \vartheta \le \pi$, and $0 \le \phi \le 2\pi$. They play the roles of radial coordinate, the colatitude angle and the azimuthal angle in spheroidal coordinates, respectively. The gradient of a scalar function $\psi(\xi, \vartheta, \phi)$ is defined by

$$\nabla\psi = \hat{\xi}\frac{1}{h_\xi}\frac{\partial\psi}{\partial\xi} + \hat{\vartheta}\frac{1}{h_\vartheta}\frac{\partial\psi}{\partial\vartheta} + \hat{\phi}\frac{1}{h_\phi}\frac{\partial\psi}{\partial\phi} \tag{4.2}$$

where the metrical coefficients are provided by

$$h_\xi = D\frac{\sqrt{\xi^2 - \cos^2\vartheta}}{\sqrt{\xi^2 - 1}} \tag{4.3a}$$

$$h_\vartheta = D\frac{\sqrt{\xi^2 - \cos^2\vartheta}}{\sin\vartheta} \tag{4.3b}$$

$$h_\phi = D\sqrt{\xi^2 - 1}\sin\vartheta \tag{4.3c}$$

Here as the far-field approximation is the main goal, it can be shown that in the limit as $\xi \to \infty$, one can replace h_ξ, h_ϑ, h_ϕ, $\hat{\xi}$ and $\hat{\vartheta}$ with D, r, $r\sin\theta$, $\hat{r}$ and $\hat{\theta}$ respectively. One can obtain the results for the oblate spheroid directly from those of the prolate spheroid by replacing all ξ_0 with $i\xi_0$ in the prolate formulas given in the following sections 4.1 and 4.2.

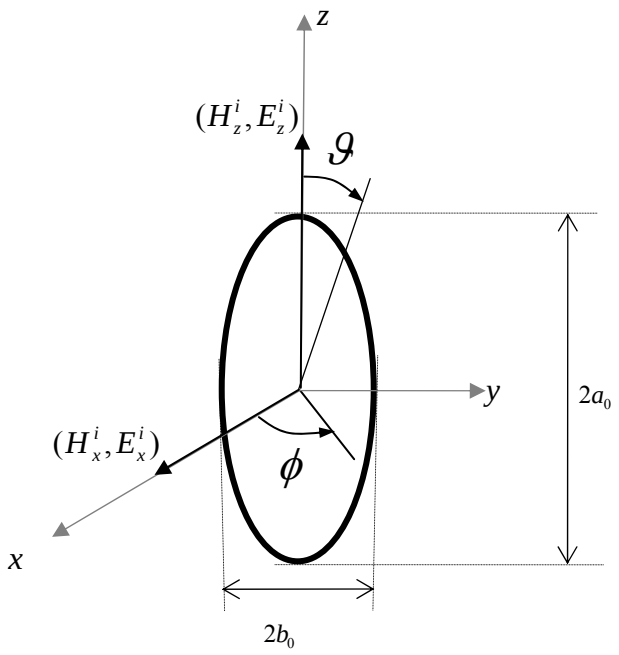

Figure 4-1: A perfectly conducting prolate spheroidal object being excited with incident electric and magnetic fields

4.1. Eddy-Current Response for a Conducting Prolate Spheroid

Similar to the spherical object, we have all the same assumptions for the uniform incident magnetic field over the extent of the conducting prolate spheroid. According to Fig. 4.1, the excitation of major and minor axes through the incident magnetic fields, $\overline{H}_z^i$ and $\overline{H}_x^i$, is assumed, respectively. Therefore finding the scattered magnetic fields, $\overline{H}_z^s$ and $\overline{H}_x^s$, for each of the excitations is required in order to compute the induced voltage in any arbitrarily-placed receiving coil pertinent to Eddy-Current response. The incident magnetic fields can be written as [41-43]

$$\overline{H}_z^i = H_z^i \hat{z} = -\nabla \psi_z^i \quad , \tag{4.4a}$$

$$\overline{H}_x^i = H_x^i \hat{x} = -\nabla \psi_x^i \tag{4.4b}$$

The manipulation of induced potentials $\psi_{z,x}^i$ from Cartesian coordinates into spheroidal ones yields

$$\psi_z^i(\xi,\vartheta) = -H_z^i D\xi\cos\vartheta = -H_z^i D P_1^0(\xi)P_1^0(\cos\vartheta) \tag{4.5a}$$

$$\psi_x^i(\xi,\vartheta) = -H_x^i D\sqrt{\xi^2-1}\sin\vartheta\cos\phi = -H_x^i D P_1^1(\xi)P_1^1(\cos\vartheta)\cos\phi \tag{4.5b}$$

Neglecting any induced currents in the outer space of the spheroid is the essence of Eddy-Current response, while equation (3.10) implies that the normal component of magnetic field over the prolate spheroid with infinite conductivity must be zero.

$$\frac{\partial}{\partial \xi}\left[\psi_{z,x}^i + \psi_{z,x}^s\right]_{\xi=\xi_0} = 0 \tag{4.6}$$

In general, the scattered potential $\psi_{z,x}^s$ can be derived through the series solution containing the first and second kind of Legendre functions as follows

$$\psi_{z,x}^s(\xi,\vartheta,\phi) = \sum_{n=0}^{\infty}\sum_{m=0}^{n}\left[A_{mn}\cos(m\phi) + B_{mn}\sin(m\phi)\right]P_n^m(\cos\vartheta)Q_n^m(\xi) \tag{4.7}$$

The symmetric solution in this problem implies that all m must be zero, then (4.7) can be reduced to

$$\psi_{z,x}^s = \sum_{n=0}^{\infty} A_n P_n(\cos\vartheta)Q_n(\xi) \tag{4.8}$$

The orthogonality of the Legendre functions and substituting (4.5a), (4.5b) and (4.8) into (4.6) give the modified solution for (4.8) as follows

$$\psi_z^s = A_1 P_1^0(\cos\vartheta) Q_1^0(\xi) \tag{4.9a}$$

$$\psi_x^s = A_{11} P_1^1(\cos\vartheta) Q_1^1(\xi)\cos\phi \tag{4.9b}$$

Solving the only unknown coefficients A_1 and A_{11}, one can obtain

$$A_1 = H_z^i D \frac{P_1^0(\xi_0)'}{Q_1^0(\xi_0)'} \tag{4.10a}$$

$$A_{11} = H_x^i D \frac{P_1^1(\xi_0)'}{Q_1^1(\xi_0)'} \tag{4.10b}$$

Through computing the gradient of scattered potentials (4.9a) and (4.9b), one can obtain the exact solution for the scattered magnetic fields. We apply the large values for the argument of Legendre functions. By using well known properties and approximation of Legendre functions [45] and replacing the metrical coefficients of spheroidal coordinates with the spherical ones as mentioned in chapter 4, the scattered magnetic fields are given as fallows

$$\overline{H}_z^s(r,\theta) = \frac{H_z^i D^3}{3} \frac{P_1^0(\xi_0)'}{Q_1^0(\xi_0)'} \frac{1}{r^3}\left[2\hat{r}\cos\theta + \hat{\theta}\sin\theta\right] \tag{4.11a}$$

$$\overline{H}_x^s(r,\theta,\phi) = \frac{2H_x^i D^3}{3} \frac{P_1^1(\xi_0)'}{Q_1^1(\xi_0)'} \frac{1}{r^3} \times \left[\hat{r}\,2\sin\theta\cos\phi - \hat{\theta}\cos\theta\cos\phi + \hat{\phi}\sin\phi\right] \tag{4.11b}$$

where $\hat{r}$, $\hat{\theta}$ and $\hat{\phi}$ are the unit vectors in spherical coordinates defined with the origin at the centre of prolate spheroid and the zenith angle is measured from the z axis.

4.2. Current-Channeling Response for a Conducting Prolate Spheroid

The geometry of the problem is similar to the Eddy-Current configuration except for the boundary condition which is different for the components of the electric field. The incident electric fields and their pertinent potentials are given as

$$\overline{E}_z^i = E_z^i \hat{z} = -\nabla \psi_z^i \tag{4.12a}$$

$$\overline{E}_x^i = E_x^i \hat{z} = -\nabla \psi_x^i \tag{4.12b}$$

The boundary condition on the surface of prolate spheroid with infinite conductivity is a zero tangential component of the electric field as

$$\hat{\xi} \times \nabla \left(\psi_{z,x}^i + \psi_{z,x}^s \right) \Big|_{\xi=\xi_0} = 0 \tag{4.13}$$

Analogous to the procedure for finding the scattered potential of magnetic fields, one can obtain the scattered potential of electric fields as fallows

$$\psi_z^s = E_z^i D \frac{P_1^0(\xi_0)}{Q_1^0(\xi_0)} Q_1^0(\xi) P_1^0(\cos\vartheta) \tag{4.14a}$$

$$\psi_x^s = E_x^i D \frac{P_1^1(\xi_0)}{Q_1^1(\xi_0)} Q_1^1(\xi) P_1^1(\cos\vartheta) \cos\phi \tag{4.14b}$$

Subsequently, computing the gradient of scattered potentials of electric fields yields the exact solution as fallows

$$\overline{E}_z^s(\xi,\vartheta) = -E_z^i D \frac{P_1^0(\xi_0)}{Q_1^0(\xi_0)} \times \left[\hat{\xi} \frac{Q_1^0(\xi)'}{h_\xi} \cos\vartheta - \hat{\vartheta} \frac{Q_1^0(\xi)}{h_\vartheta} \sin\vartheta \right] \tag{4.15a}$$

$$\overline{E}_x^s(\xi,\vartheta,\phi) = -E_x^i D \frac{P_1^1(\xi_0)}{Q_1^1(\xi_0)} \left[\hat{\xi} \frac{Q_1^1(\xi)'}{h_\xi} \sin\vartheta\cos\phi + \hat{\vartheta} \frac{Q_1^1(\xi)}{h_\vartheta} \cos\vartheta\cos\phi - \hat{\phi} \frac{Q_1^1(\xi)}{h_\phi} \sin\vartheta\sin\phi \right] \tag{4.15b}$$

Owing to the conductivity of background medium surrounding the prolate spheroid, the scattered electric fields have their associated magnetic fields which must satisfy the equation (3.15). Therefore using the approximation of Legendre functions [45] and the substitution of unit vectors with their corresponding ones in spherical coordinates, one can obtain

$$\overline{\widetilde{H}}_z^s(r,\theta) = \hat{\phi} \frac{\sigma_0 E_z^i D^3}{3} \frac{P_1^0(\xi_0)}{Q_1^0(\xi_0)} \frac{\sin\theta}{r^2} \tag{4.16a}$$

$$\overline{\widetilde{H}}_x^s(r,\theta,\phi) = -\frac{2\sigma_0 E_x^i D^3}{3} \frac{P_1^1(\xi_0)}{Q_1^1(\xi_0)} \frac{1}{r^2} \left[\hat{\theta}\sin\phi + \hat{\phi}\cos\theta\cos\phi \right] \tag{4.16b}$$

4.3. Polarizability for Prolate Spheroid towards its Aspect Ratio a/b

The shape of a prolate spheroid is determined by the lengths of its semimajor and semiminor axes a and b with $(a \geq b)$. Again we recall that the "ellipticity" of the prolate spheroid is defined by $e \equiv \sqrt{a^2 - b^2}/a$ where $0 \leq e < 1$ and $e = 0$ implies a sphere.

Now suppose a conducting sphere with a radius equal to the length of the semi major axis of a conducting spheroid, i.e., the volume of the spheroid $\left(4/3\,\pi b^2 a\right)$ is always less than that sphere $\left(4/3\,\pi a^3\right)$. In this case the Eddy-Current response and Current-Channeling response of the conducting spheroid are expressed relative to that of a conducting sphere of radius a. The coefficients $\alpha_{EC}^{(A)}, \alpha_{EC}^{(T)}, \alpha_{CC}^{(A)}$ and $\alpha_{CC}^{(T)}$ are referred to as "magnetic polarizabilties" and compare the ECR and CCR of a conducting spheroid with a conducting sphere with the same semi major axis and radius.

In the following, $P_1^0(\xi_0), P_1^1(\xi_0)$, $Q_1^0(\xi_0)$ and $Q_1^1(\xi_0)$ are Legendre functions of the first and second kinds with argument $\xi_0 \equiv a/\sqrt{a^2-b^2} = 1/e$. In fact the Legendre functions can be expressed in terms of elementary functions (see Appendix B).

In a conducting prolate spheroid we found the effect of Eddy-Current just due to the incident magnetic field by $V_{EC}^{(A)} = \alpha_{EC}^{(A)} V_{EC}^{(Sphere)}$ and $V_{EC}^{(T)} = \alpha_{EC}^{(T)} V_{EC}^{(Sphere)}$. Here we have derived the exact formula for $\alpha_{EC}^{(A)}, \alpha_{EC}^{(T)}$ by utilizing the Legendre functions of the first and second kinds where

$$\alpha_{EC}^{A} \equiv -\frac{2}{3\xi_0^3}\frac{P_1^{0\prime}(\xi_0)}{Q_1^{0\prime}(\xi_0)} = \frac{2}{3}\left[\frac{e^3}{\frac{e}{1-e^2}-\frac{1}{2}\ln\left(\frac{1+e}{1-e}\right)}\right] \tag{4.17a}$$

$$\alpha_{EC}^{T} \equiv -\frac{4}{3\xi_0}\frac{P_1^{1\prime}(\xi_0)}{Q_1^{1\prime}(\xi_0)} = \frac{4}{3}\left[\frac{e^3}{\frac{1}{2}\ln\left(\frac{1+e}{1-e}\right)+\frac{e^3}{1-e^2}-e}\right] \tag{4.17b}$$

Fig. 4.2 shows a graph of the Eddy-Current polarizabilities for prolate spheroids as a function of the aspect ratio a/b with respect to a sphere with radius a .

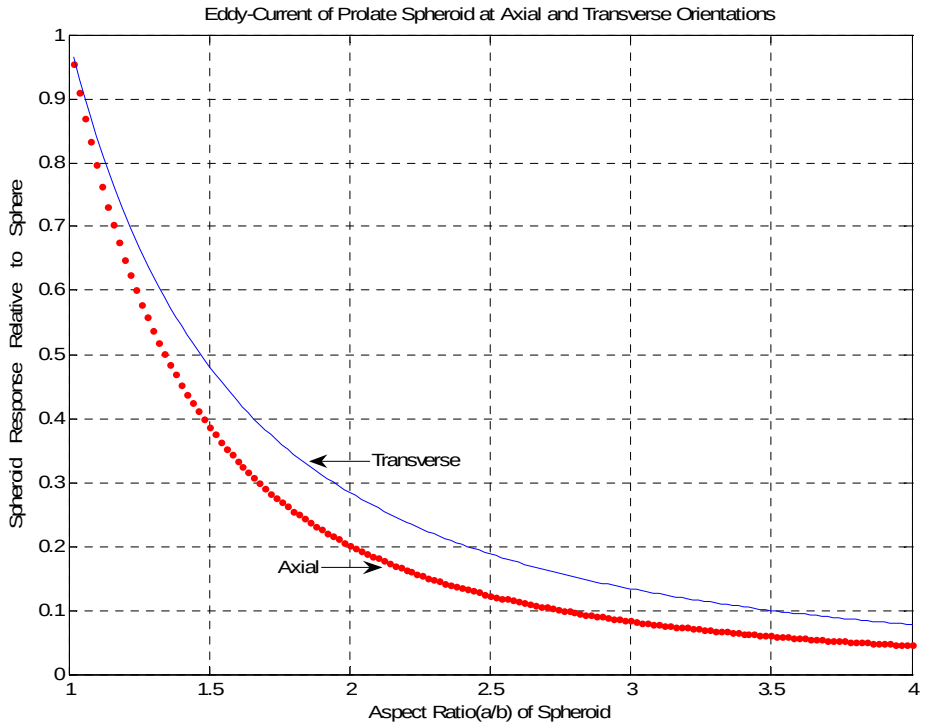

Figure 4-2: Eddy-current polarizibilites of Prolate at two orientations

The main point should be noted is that, as the aspect ratio of the spheroid increases, the axial eddy-current response falls slightly more rapidly than the transverse eddy-current response.

We have the same formula as above for the Current-Channeling response just due to the incident electric field for the conducting prolate spheroid $V_{CC}^{(A)} = \alpha_{CC}^{(A)} V_{CC}^{(Sphere)}$ and $V_{CC}^{(T)} = \alpha_{CC}^{(T)} V_{CC}^{(Sphere)}$ where

$$\alpha_{CC}^{A} \equiv \frac{1}{3\xi_0^3} \frac{P_1^0(\xi_0)}{Q_1^0(\xi_0)} = \frac{1}{3}\left[\frac{e^3}{\frac{1}{2}\ln\left(\frac{1+e}{1-e}\right) - e}\right] \tag{4.18a}$$

$$\alpha_{CC}^{T} \equiv \frac{2}{3\xi_0^{\,3}} \frac{P_1^1(\xi_0)}{Q_1^1(\xi_0)} = \frac{2}{3}\left[\frac{e^3}{\frac{e}{1-e^2} - \frac{1}{2}\ln\left(\frac{1+e}{1-e}\right)}\right] \tag{4.18b}$$

Fig. 4.3 shows a graph of the Current-Channeling polarizabilities for prolate spheroids as a function of the aspect ratio a/b with respect to a sphere with radius a.

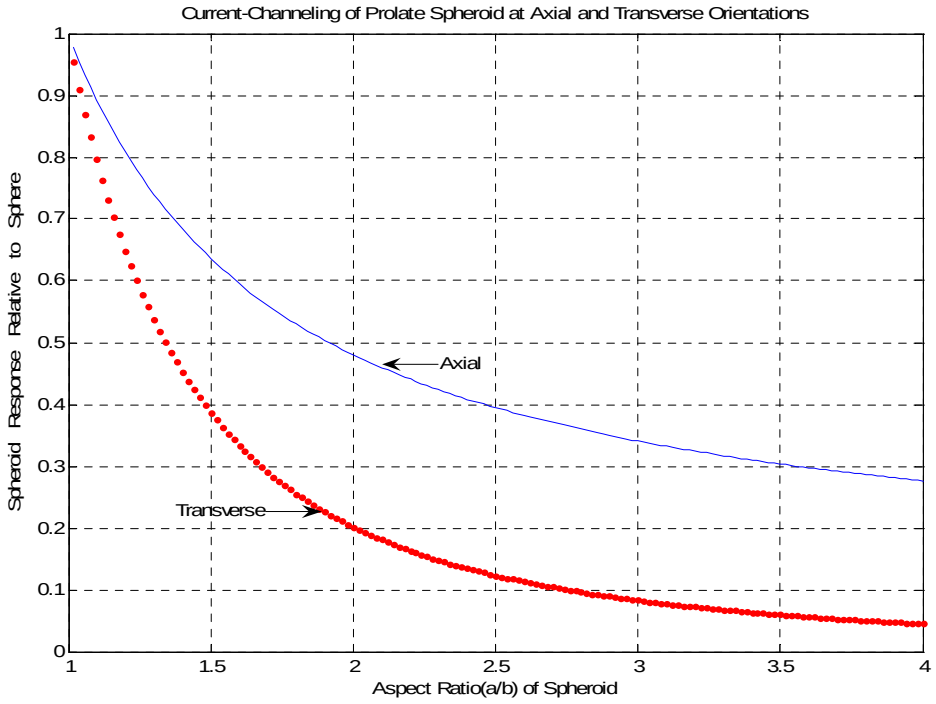

Figure 4-3: Current-Channeling polarizibilites of Prolate at two orientations

The main point in the graph is that the axial current-channeling response is always larger than the transverse current-channeling response.

It should be noted that these EMI responses to spheroidal objects are in weakly conducting medium. In fact, "weakly conducting" implies that the depth penetration of electromagnetic fields in the background is large compared to the size of the spheroid. The main point in these graphs is that these polarizability factors are independent of frequency ranges. In fact, it is a

comparison coefficient which can be applied in any frequency and just the geometry of the spheroid specifies its value. As is seen in the figures 4.2 and 4.3, the value of $\alpha_{EC}^{(A)}, \alpha_{EC}^{(T)}, \alpha_{CC}^{(A)}$ and $\alpha_{CC}^{(T)}$ are always less than 1.

4.4. Effect of Different Orientations of a Prolate Spheroid in the Induced Voltage

Most of the concealed mines, especially the marine mines, do not have a fixed orientation with regard to the horizontal surface of the area where they are discovered [14]. As it was found in sections 4.1 and 2.2, the behavior of scattered fields of a spheroidal object is analogous to that of the spherical object in the far field. What causes the induced voltage of a spheroidal mine to be different from a spherical mine pertains to its symmetry axis orientation and the ratio of the semi major axis to its semi minor one. Three representative modes of embedding a spheroidal mine in the conducting medium are considered in the Figures 4.4, 4.5 and 4.6 respectively. The components of the incident fields used to excite the axes of the spheroid are computed similar to the sphere by equations (3.9a) and (3.9b). Turning the symmetry axis of the transmitting coil on the $x'z'$ plane is a mutual assumption among all the cases and suppressed throughout.

4.4.1. Vertical Prolate Spheroid with Long Axis Perpendicular to the Surface

As shown in Fig. 4.4 the long axis of the prolate spheroid is in the same plane on which the symmetry axis of the receiving coil is laid. Through utilizing the scattering magnetic fields separately for any component of the incident fields, H_r^i , H_θ^i and E_ϕ^i, one can find the induced

voltage in the receiving coil corresponding to each element. By applying the equations (4.11a), (4.11b) and (3.13), the Eddy-Current response due to the incidents magnetic fields, is given by

$$V_{EC}^{pro}\left(d_t,\xi_0,\theta_T\right)=i\frac{N_T N_R A_T A_R I_T \omega\mu_s D^3}{6\pi d_t^{\,6}}\left(\frac{2P_1^0\left(\xi_0\right)'}{Q_1^0\left(\xi_0\right)'}\cos^2\theta_T+\frac{P_1^1\left(\xi_0\right)'}{Q_1^1\left(\xi_0\right)'}\sin^2\theta_T\right) \qquad (4.19a)$$

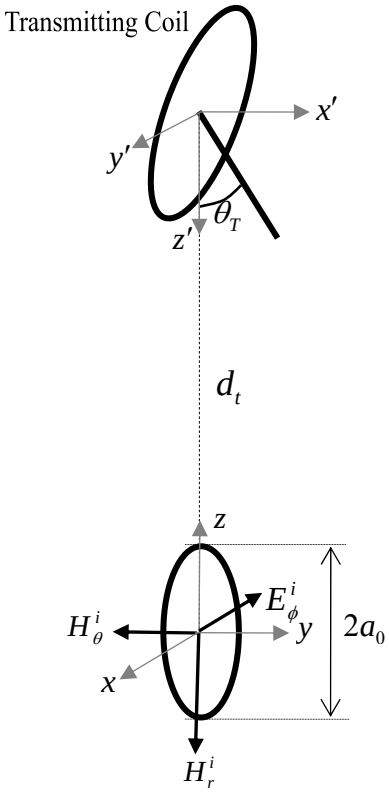

Figure 4-4: The first representative modes of a spheroidal mine embedded in the conducting medium

Subsequently, the induced Current-Channeling response owing to the incident electric field is computed by substituting (4.16b) into (3.13).

$$V_{CC}^{pro}\left(d_t,\xi_0,\theta_T\right)=\frac{N_T N_R A_T A_R I_T \omega^2\mu_s^{\,2}\sigma_0 D^3}{6\pi d_t^{\,4}}\left(\frac{P_1^1\left(\xi_0\right)}{Q_1^1\left(\xi_0\right)}\sin^2\theta_T\right) \qquad (4.19b)$$

4.4.2. Horizontal Prolate Spheroid with Long Axis Parallel to Symmetry Axis of the Coil

Fig. 4.5 shows how horizontally the prolate spheroid is laid while its long axis is parallel to the symmetry axis of the receiving coil. The displacement of the long axis of the spheroid in this case is what the slight difference in total response towards the vertical spheroid results from. Thus the Eddy-Current response is computed similar to the vertical mode by using the equations (4.11a), (4.11b) and (3.13).

$$V_{EC}^{pro}(d_t,\xi_0,\theta_T)=i\frac{N_T N_R A_T A_R I_T \omega\mu_s D^3}{12\pi d_t^{\,6}}\left(\frac{8P_1^1(\xi_0)'}{Q_1^1(\xi_0)'}\cos^2\theta_T+\frac{P_1^0(\xi_0)'}{Q_1^0(\xi_0)'}\sin^2\theta_T\right) \qquad (4.20a)$$

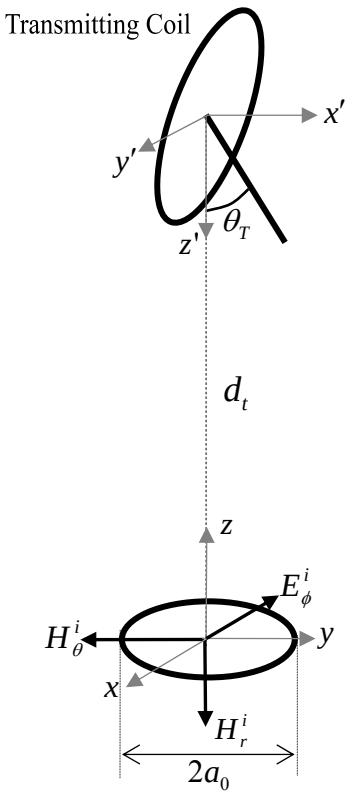

Figure 4-5: The second representative modes of a spheroidal mine embedded in the conducting medium

The electric field exciting the major axis of the spheroid generates an induced electrical current along the minor axis on the surface of the conducting spheroid. The consequence of the induced current is a perturbation in the surrounding conducting medium. Due to this perturbed current in the medium, the Current-Channeling response is found through utilizing (4.16b) into (3.13).

$$V_{CC}^{pro}\left(d_t,\xi_0,\theta_T\right)=\frac{N_T N_R A_T A_R I_T \omega^2 {\mu_s}^2 \sigma_0 D^3}{6\pi {d_t}^4}\left(\frac{P_1^1\left(\xi_0\right)}{Q_1^1\left(\xi_0\right)}\sin^2\theta_T\right) \tag{4.20b}$$

4.4.3. Horizontal Prolate Spheroid with Long Axis Perpendicular to Symmetry Axis of the Coil

The rotation of the previous horizontal conducting spheroid around its minor axis brings about Fig. 4.6 in which the zenith component of the incident magnetic field is aligned along the minor axis of the conducting prolate spheroid. Similarly to the vertical spheroid both major and minor axes are exposed to the incident magnetic fields, thus the Eddy-Current response in this mode is coming from equations (4.11b) and (3.13) as follows

$$V_{EC}^{pro}\left(d_t,\xi_0,\theta_T\right)=i\frac{N_T N_R A_T A_R I_T \omega \mu_s D^3}{6\pi {d_t}^6}\left(\frac{4P_1^1\left(\xi_0\right)'}{Q_1^1\left(\xi_0\right)'}\cos^2\theta_T+\frac{P_1^1\left(\xi_0\right)'}{Q_1^1\left(\xi_0\right)'}\sin^2\theta_T\right) \tag{4.21a}$$

The principal distinction between this mode and the two previous ones refers to the direction of the incident electric field which causes a considerable electrical current along the long axis of the conducting prolate spheroid. Owing to the appropriate orientation of the receiving coil with

respect to the spheroid, this term can have an essential effect on the total response. By utilizing equations (4.16a) and (3.13), the Current-Channeling response is given by

$$V_{CC}^{pro}(d_t,\xi_0,\theta_T)=\frac{N_T N_R A_T A_R I_T \omega^2 {\mu_s}^2 \sigma_0 D^3}{12\pi {d_t}^4}\left(\frac{P_1^0(\xi_0)}{Q_1^0(\xi_0)}\sin^2\theta_T\right) \tag{4.21b}$$

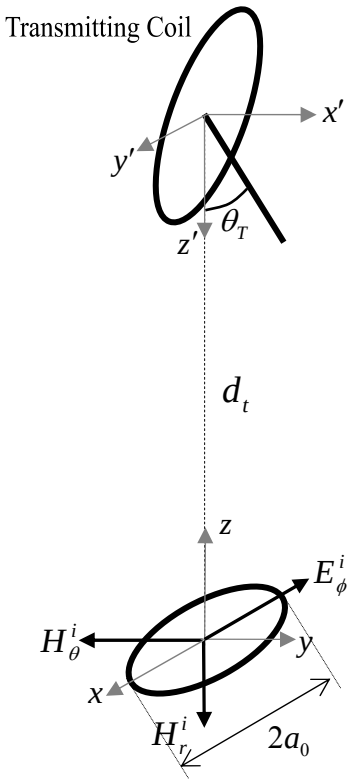

Figure 4-6: The third representative modes of a spheroidal mine embedded in the conducting medium

We wish to point out that the vertical orientation of the spheroidal mine is independent of the deviation angle of the transmitting coil axis. Only the horizontal positions of the spheroidal mine with respect to the transmitting coil axis will affect the induced voltage. We have considered the two main positions of the spheroidal mine in which the electric field component is directed both along the major and minor axes of the spheroid in two separate cases. The method can be extended to an arbitrary oriented spheroidal object, by decomposing the components of the

electric and magnetic fields, respectively, along the major and minor axes of the spheroidal object.

4.5 Conclusion

In this chapter, we could compare the backscattered induced EMF response of a spheroid with a sphere of the same radius and then demonstrate the pertinent derivations for spheroidal mines with unified coils. We showed that the aspect ratio of spheroid and its orientation with respect to the receiving coil can dominantly affect on the ECR and CCR. The importance of these effects can be disclosed in a factor which is called the "polarizibility" factor. In order to expand our scheme for a wide range of conducting marine mines with different volumes and orientations, we used three modes of embedding a spheroidal mine in the conducting medium. The magnificence of this approach with respect to the previous works is that the relation between the total induced voltages in the receiving coil due to a spheroidal marine mine is analogous to its corresponding spherical marine mine which can satisfy the conditions mentioned in this chapter already.

Chapter 5. Numerical Results and Discussion

Consider a GEM-3 sensor [25] in which the transmitting and receiving coils in the Fig. 3.2 are in the same location and orientation with respect to the marine mine. Therefore $\alpha_\theta^s = \alpha_\phi^s = 90^0$, $\alpha_r^s = 180^0$ and $\theta_T = \theta_R = \theta_0$. A marine mine with $2a_0 = 10cm$ is assumed to be positioned at distance $d_t = d_r = d_0$ from the GEM-3 set at the frequency of $20\,kHz$. The most common mines found in water are composed of metals and explosive. The constitutive parameters of seawater are assumed to be $\mu_s = \mu_0$ and $\sigma_s = 4S/m$ [12]. Fig. 5.1 shows the angular scan of the normalized total induced voltage in the receiving coil on account of both ECR and CCR, through rotating the angle of symmetry axis of the coils, θ_0, from 0 to 90 degrees with respect to the marine mine positioned at different values of d_0 from the sensor. These angular scans can be used to detect the unknown location of the marine mine.

In such low frequency application, the entire objects behave similarly to a magnetic dipole like a spheroidal conducting object. The differences between the induced voltages due to various conducting objects are their shapes and orientations.

5.1. Results for Spherical Mine Detection

Our results refer to the measurements carried out above the mine's location. In practice, it is not a hurdle to position the transmitting coil above the mine because the common concentric sensors receive the maximum secondary magnetic field exactly at top of the mine. Afterwards

we can apply our proposed scheme to find the depth of the mine. It is a presumption in different schemes that the measurements are carried out above the buried mines as given in references [12, 14, 15, and 38].

According to the equations (3.14) and (3.17), it is worth noting that the normalized induced voltage in Fig. 5.1 has a trivial sensitivity to the size of common marine mines and is appropriate for common metallic spherical mines. After finding the depth of the marine mine by the equations (3.14) and (3.17), the absolute induced voltage could provide additional data on the approximate size of the marine mine. Owing to the conductivity of sea water that perturbs the induced currents, higher operating frequencies can amplify the CCR, similarly, through higher distances from the sensor, CCR can substantially exceed ECR.

Fig. 5.1 is also depicting that the maximum ECR is obtained when the marine mine is on the symmetry axis of the transmitting coil. On the other hand, the CCR has a zero value on this axis and its maximum occurs at 90° from the symmetry axis. In sections 4.1 and 4.2, the similarity between the far-field approximations of scattered fields of a conducting spheroidal object and a spherical one demonstrates that applying this methodology for different orientations of a spheroidal mine will lead to obtaining results for a conducting spheroidal mine analogous to Fig. 5.1. Thus, in order to customize Fig. 5.1 for a prolate spheroidal object and then utilize it to make a better depth detection, it is merely necessary to investigate the influences of axes aspect ratio, depth and orientation of a conducting spheroidal mine on the induced voltage in the receiving coil relative to a spherical one.

It is worth mentioning that the accuracy of the normalized graph is sensitive to the depth of the mine. In general, for lower depth, we have access to the stronger secondary magnetic field and

this leads to an accurate normalized graph versus the angle θ_T . However, for higher depths the absolute value of induced voltage is relatively weak and makes the detection of mine's depth a more challenging task.

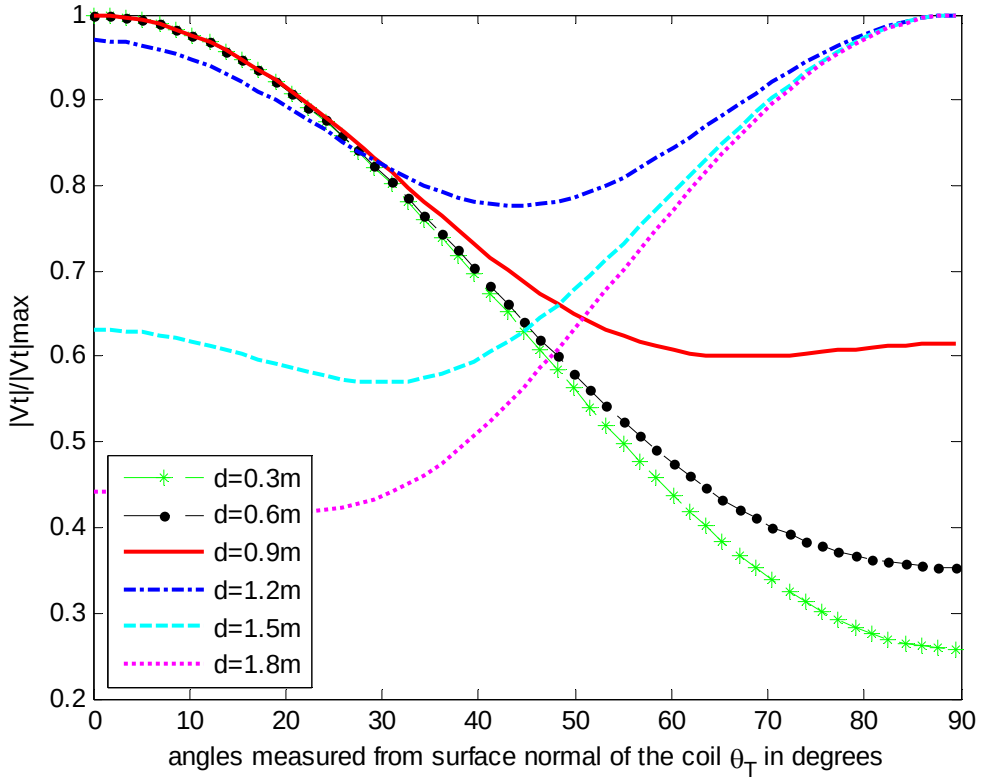

Figure 5-1: Angular scan of normalized induced voltage for a spherical conducting marine mine at different depths

5.2. Enhanced Spheroidal Mine Depth Detection

In the following comparison, we assume a conducting spheroidal mine with a major axis equal to the sphere diameter, while the only variable factor is the minor axis of spheroid varying according to its corresponding sphere. Fig. 5.2 depicts how the depth of the buried conducting spheroid shown in Fig. 4.4 with the axes aspect ratio of 0.6 can affect the total induced voltage in

the receiving coil relative to its corresponding sphere at any specific angle. Between the scanning angles of 0 to 40 degrees, all the curves nearly overlay, which indicates that the ECR due to the radial component of incident magnetic field has more influential impact on the total induced voltage than the other factors. By decreasing the depth of the buried conducting spheroid, one can find that its total induced voltage increasing rate against the scanning angle increment is higher than that of the corresponding spherical one. It shows that such vertical configuration for a conducting spheroidal mine buried in lower depth has a more sensitive Current-Channeling response relative to the corresponding one at higher depth. In fact the effect of CCR as applied to the conducting environment can significantly affect the detection range. The absolute value of CCR can dominate the ECR at a higher depth as it has a decay rate proportional to $1/d^4$, while the ECR has a decay rate proportional to $1/d^6$.

It is worth mentioning that when the responses of the conducting spheroids are compared to that of the enclosing spheres, the relative response is always less than 1 as the fundamental consequence of these comparisons. The best interpretation of this behavior is that in the low frequencies applied to the marine mine detection, both spheres and spheroids respond as magnetic dipoles, hence spheres with larger volumes have more effective induced response compared with their corresponding spheroids.

By our method if one does the angular scanning exactly above the buried object, it will be found a monotonically increasing or decreasing curve versus θ_T, otherwise the normalized graph is not monotonic and has a maximum or minimum point at least at a specific θ_T. Suppose that the center of the transmitting coil has been deviated by 30^0 from the object buried at the depth of 0.85 m. Therefore the coil should be relocated approximately 50 cm to be positioned above the

mine. If our method is applied to this case, by scanning the θ_T from 0^0 to 30^0 one has an increasing curve and then by increasing the θ_T from 30^0 to 90^0 it would be found a decreasing curve. The maximum point in the measured data shows that how far the transmitting coil has been deviated from the buried object. For the depth higher than 1 meter we have the same scenario but there would be a minimum point instead of the maximum point for detecting the deviation angle.

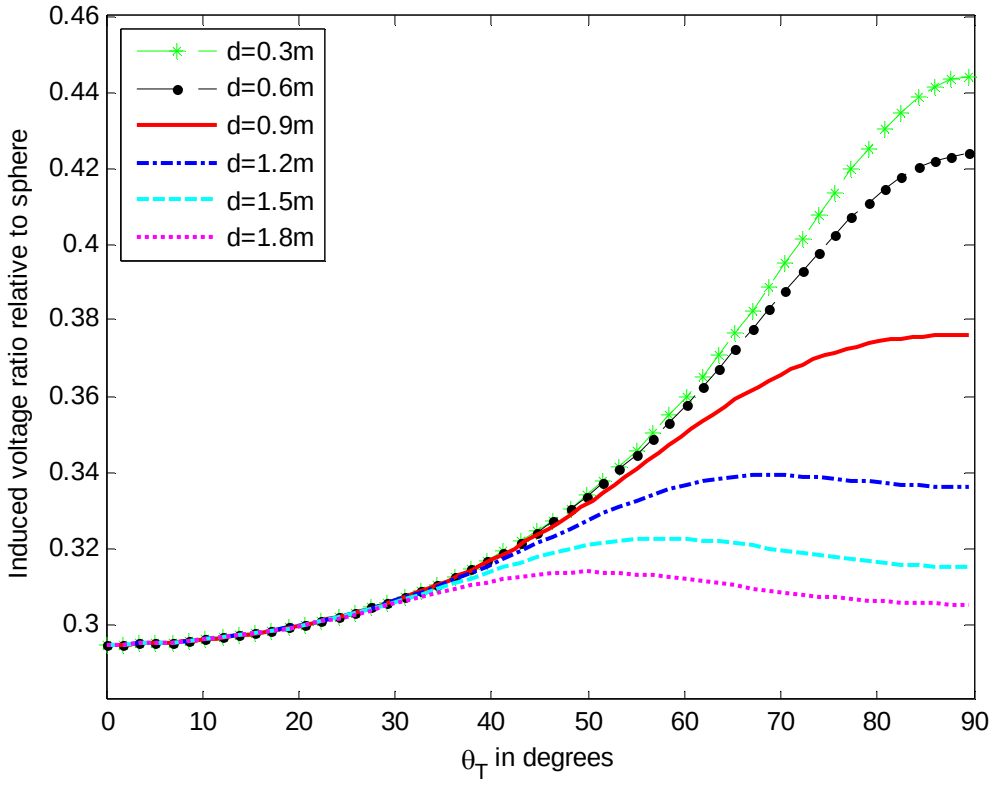

Figure 5-2: Angular scan of the total induced voltage for a conducting spheroid relative to its corresponding sphere with the axes aspect ratio of 0.6 at different depths for the configuration depicted in Figure 4.4

Figures 5.3 and 5.4 show the results for the two common deploying configurations of spheroidal mines depicted in Fig. 4.5 and Fig. 4.6, respectively. The patterns are observed in Fig. 5.3 and Fig. 5.4 through the increase on the scanning angle from $\theta_0 = 40^0$. They can be

associated with the angles in which the CCR exceeds the ECR level and this demonstrates that CCR can enhance the discrimination capability in greater depth as well as the ECR does in the lower depth. What is more significant in Fig. 4.6 in comparison to the first two modes is the efficient orientation of the major axis which leads to the higher induced voltage regarding the other configurations. As shown in Fig. 4.6, both radial and zenith components of incident magnetic fields excite the long axis of the spheroid, thus the receiving coil is being excited through a larger part of the spheroid. The effectiveness of CCR is more apparent in Fig. 5.4 in relation to the other modes, because the electrical incident field is parallel to the long axis, thus the induced electrical current is provided with the longest path for flowing through the conducting spheroid.

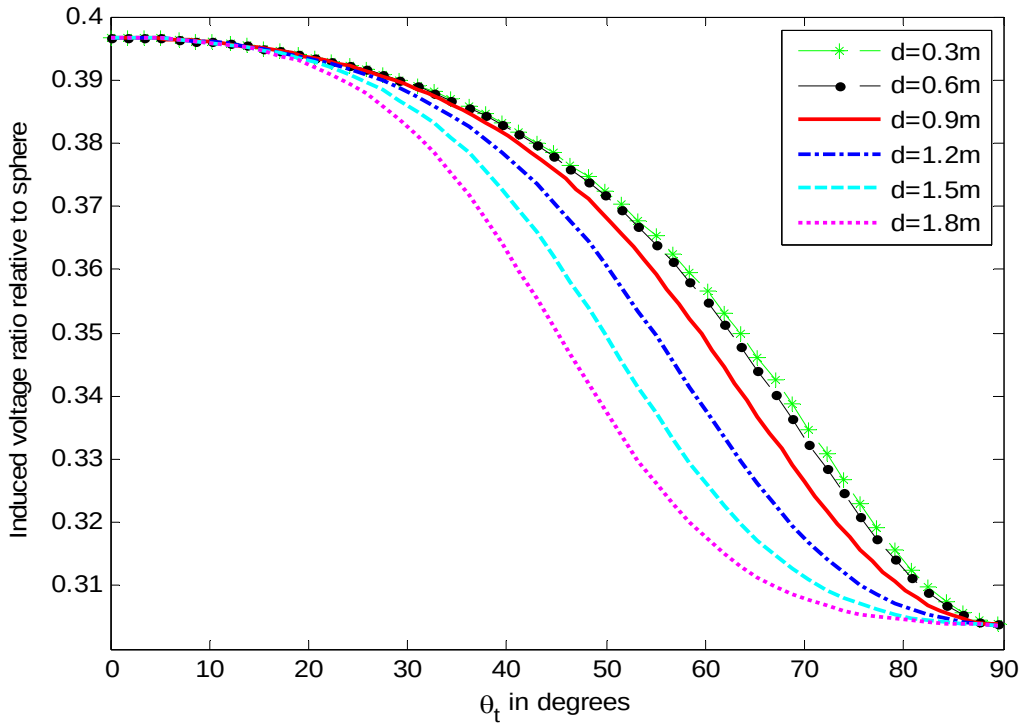

Figure 5-3: Angular scan of the total induced voltage for a conducting spheroid relative to its corresponding sphere with the axes aspect ratio of 0.6 at different depths for the configuration depicted in Figure 4.5

To determine the unknown depth of the buried object, the effects of both CCR and ECR are taken into account simultaneously in our scheme. This approach leads to a considerable enhancement up to about 2m in detection range while the other schemes presented in [25, 41] rely on each of ECR and CCR separately.

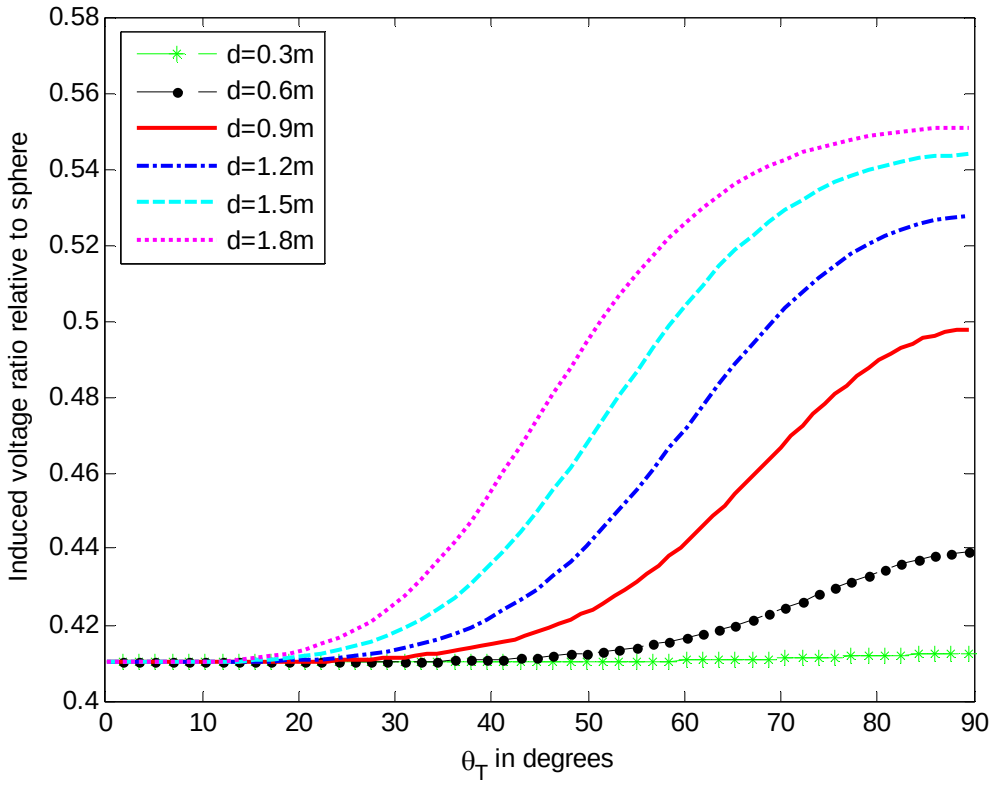

Figure 5-4: Angular scan of the total induced voltage for a conducting spheroid relative to its corresponding sphere with the axes aspect ratio of 0.6 at different depths for the configuration depicted in Figure 4.6

Fig. 5.5 shows how the axes aspect ratio of the conducting spheroid depicted in the Fig. 4.4 can affect the induced response in the receiving coil relative to the corresponding sphere at the depth of $d_0 = 0.9m$. By decreasing the aspect ratio b/a towards zero, it is found that the relative response tends towards zero too. In fact the spheroid stretches into a long thin rod while the

aspect ratio b/a tends to zero and consequently the effective surface of the conducting spheroid acting as the scatterer decreases. The spheroid with an axes aspect ratio of $b/a = 0.99$ has the most similar response to its corresponding sphere.

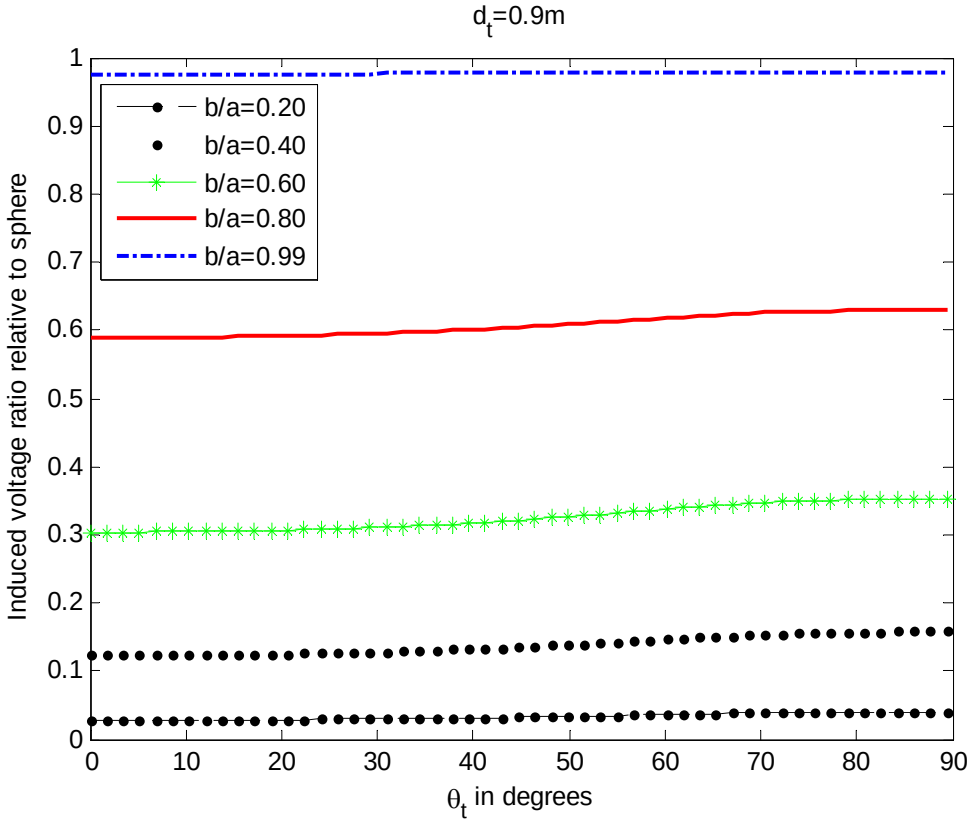

Figure 5-5: Angular scan of the total induced voltage for a conducting spheroid buried vertically relative to its corresponding sphere with different axes aspect ratio for the depth dt=0.9m

5.3 Conclusion

In this chapter we initially showed that how accurately the normalized total induced voltage in the receiving coil can be applied for the detection of spherical marine mine's depth. Our method could gain competence in a wide range of mine geometries because of using three different orientations of spheroidal mines. The results prove that the angular scanning of transiting coil

brings about a reliable approach to detect the depth of spheroidal marine mines. On the other hand the aspects ratio of axes in the spheroidal conducting mines revealed that this factor has much more effect on the total induced voltage rather than the deviation angle in the transmitting coil.

Chapter 6. Conclusion and Future Work

6.1. Conclusion

We have presented a novel scheme which is able to determine the location and depth of a metallic mine embedded in a conducting medium on the foundation of Eddy-Current and Current-Channeling responses which can be measured with both separate and concentric transmitting and receiving coils for spherical and spheroidal conducting marine mines, respectively. This technique is based on the uniqueness of the normalized induced voltages measured at different depths through scanning the angle of which the transmitter symmetry axis is displaced from the marine mine. The previous researchers presented the induced voltage in the receiving coil merely due to the radial component of the incident magnetic fields. They also have simplified the problem by ignoring the effect of H_{θ}^{i}. Our results showed that this component has a considerable effect on the total induced voltage especially in the case of CCR. In addition, we have also expanded a new model for the separate transmitting and receiving coil measurement.

Using some modifications in the normalized graphs through considering the influences of depth, orientation and axes aspect ratio of the spheroid as the fundamental factors, the customized graphs obtained for the conducting spheroidal mines are applicable to variable-depth mine detection as efficiently as spherical mines. We have also taken into account all of the incident electric and magnetic fields simultaneously in order to compute the total induced

voltage for any arbitrary angles by which the symmetry axis of the coil is displaced from the conducting spheroidal object. It is found that, in addition to the higher depth which strengthens the magnitude of CCR with respect to the ECR, increasing the scanning angle of the symmetry axis of the coil produces similar results. Furthermore, it is also found that the maximum detection depth in the conducting medium, like coastal seawater or marine environment, can be reached up to about $2m$. It is worth mentioning that detectable input voltage level for a modern low-noise amplifier is about 2×10^{-9} volts while the magnetic flux of the transmitting coil is adjusted by the electrical current flowed through the loops of wire [12].

6.2. Future Work

The effect of realistic noise can mask any attempt to discriminate one signal from another. Assuming classification turns out to be practical for the noiseless case, the simulation should be repeated for the same cases with typical noise in the environment. In this project, we assumed the effects of noise due to the background medium can be neglected. The effect of typical noise will be explored in the future work.

In the next step for our future work, there are some areas of working that can improve our method. In fact in all the results of chapter 5 and analytical solutions of chapter 4 we have supposed that the background medium in which object has been immersed, is homogeneous and lossless and we have the assumption of having a skin depth higher than the target size; i.e., the frequency is low enough or the object has small dimensions. Therefore, the first step is to

consider the effect of lossy medium in our analytical solution and find the exact answer for it. Meanwhile numerical methods can help us in solving such problems.

The assumption of zero displacement current or $-i\omega\varepsilon E = 0$ in analytical solution is not always valid, because if we can't access to a considerable loss tangent, then the displacement current becomes an effective factor in our solution. We can check this effect in analytical solution, too.

Another point that is valuable to be mentioned is that the boundary between the free space and host medium has been supposed to be smooth, but in reality the roughness is a factor that can act like the clutter in EMIS method. To the best of my knowledge, small-perturbation method (SPM) for rough surface scattering has been derived, recently [46]. The main idea of this work is to pose a geometrical spatial sample as one of the surface particle, and then by extending it as a periodic function for all points of the surface we can access to the behavior of all surfaces. The analytical solution has been found for this problem [46].

BIBLIOGRAPHY

1. L. Tsang, and R. T. Shin, Theory of Microwave Remote Sensing*. John Wiley & Sons, Inc.,* 1985
2. L. Yujiri, and M. Shoucri, "Passive Millimeter Wave Sensors for Detection of Buried Mines*" SPIE,* 1995. 2496
3. L. S. Riggs, "Overview of the Fundamental Operating Characteristics of the AN/PSS-12", Technical Report, JUXOCO, February 1999.
4. Technical Publication containing Preventive and Corrective Maintenance Instructions for the AN-19/2 Mine Detecting Set, Schiebel Corporation, NSN 6665-21-906-1023, June 10, 1995.
5. L. T. Lowe , "Simulants and Surrogates For Low-metal Content Landmines" Master's Thesis, Auburn University, Alabama. 1998.
6. L. S. Riggs, L. T. Lowe, J. Elkins, T. Barnett, and D. Weaver, "Discrimination Between Buried Metallic Mines and Metallic Clutter Using Signal Energy and Exponential Decay Rates," Proceedings of SPIE, Detection and Remediation of Mines and Minelike Targets V, Vol. 4038, 2-13, April 2000.
7. C.P. Gooneratne, and G. Sen Gupta, "A Review of Sensing Technologies for Landmine Detection: Unmanned Vehicle Based Approach*" International Conference on Autonomous and Agents*, 2004
8. C. E. (Ed.) Baum, Detection and Identification of Visually Obscured Targets, Taylor and Francis, Philadelphia, 1999.

9. H. A. Trang, “Simulation of Mine Detection Over Dry Soil, Snow, Ice, and Water*” SPIE, 1996.* 2765

10. P. Church, et al., “Electrical Impedance Tomography*”.* 2005

11. F. S. Grant, and G. F. West, *Interpretation Theory in Applied Geophysics*. McGraw-Hill Book Company. New York. 1965

12. I. J. Won, S. Norton, B. SanFilipo and F. Funak, “Active Broadband Electromagnetic Detection and Classification of Buried Naval Mines,” *MTS/IEEE Oceans apos,* Vol. 2, 966 – 973, Oct. 2002

13. R. Wu, J. Liu, T. Li, Q. Gao, H. Li and B. Zhang, “ Progress in the research of ground bounce removal for landmine detection with ground penetrating radar,” *Progress In Electromagnetics Research Symposium*, 22-26, China, August 2005

14. I. J. Won, D. A. Keiswetter and T. H. Bell, “Electromagnetic Induction Spectroscopy for Clearing Landmines,” *IEEE Trans. Geoscience and Remote Sensing*, Vol. 39, 703-709, Apr 2001

15. T. H. Bell, B. Barrow, and N. Khadr, “Shape-Based Classification on Discrimination of Subsurface Objects using Electromagnetic Induction” International Geoscience and remote sensing Symposium (IGARSS 98), Seattle, Washangton, july 1998.

16. K. C. Tiwari , D. Singh and M. K. Arora, “Development of a model for detection and estimation of depth of shallow buried non-metallic landmine at microwave x-band frequency,” Progress In Electromagnetics Research, PIER 79, 225-250, 2008

17. J. P. Fernandez, K. Sun, B. Barrowes, K. O’Neill, I. Shamatava, F. Shubitidze and K. Paulsen, “Inferring the location of buried UXO using a support vector machine,” *Proc SPIE*, Orlando Florida, April 11-12, Vol. 6553, 2007

18. P. B. Weichman, and E. M. Lavely, "Study of inverse problems for buried UXO discrimination based on EMI sensor data" , *Proceedings of the SPIE,* Vol. 5089, 1189-1200, 2003

19. Y. Sun, X. Li and J. Li, "Practical landmine detector using forward-looking ground penetrating radar," *Electronics Letters*, Vol. 41, 97-98, Jan 2005

20. K. Moustafa, and K. F. A. Hussein, "Performance evaluation of separated aperture sensor GPR system for land mine detection," *Progress In Electromagnetics Research*, PIER 72, 21-37, 2007

21. S. H. Zainud-Deen, M. E. Badr, E. El-Deen, K. H. Awadalla and H. A. Sharshar, "Microstrip antenna with corrugated ground plane surface as a sensor for landmines detection," *Progress In Electromagnetics Research B*, Vol. 2, 259-278, 2008

22. M. Sato, Y. Hamada, X. Feng, F. Kong, Z. Zeng and G. Fang, "GPR using an array antenna for landmine detection," *Near Surface Geophysics*, 3-9, 2004

23. M. Nishimoto, S. Ueno and Y. Kimura, "Feature extraction from GPR data for identification of landmine-like objects under rough ground surface," *Journal of Electromagnetic Waves and Applications*, Vol. 20, No. 12, 1577-1586, 2006

24. L. Carin, I. J. Won, and D. Keiswetter, "Wideband frequency- and time-domain EMI for mine detection" Proceedings of SPIE, Detection and Remediation of Mine and Minelike Targets V, Vol. 3710, 14-25, April 1999.

25. B. SanFilipo, S. Norton and I. J. Won, "The effects of seawater on the EMI response of UXO," *MTS/IEEE Oceans,* Vol.1, 607-614, 2005.

26. I. V. Lindell, and A. H. Sihvola, "Reflection and Transmission of Waves at the Interface of Perfect Electromagnetic Conductor (PEMC**)**" *Progress In Electromagnetics Research B*, Vol. 5, 169-183, 2008.

27. L. Xu, Y. C. Guo and X. W. Shi, "Dielectric half space model for the analysis of scattering from objects on ocean surface," *Journal of Electromagnetic Waves and Applications*, Vol. 21, No. 15, 2287-2296, 2007

28. O. M. Abo-Seida, "Far-field due to a vertical magnetic dipole in sea," *Journal of Electromagnetic Waves and Applications*, Vol. 20, No. 6, 707-715, 2006.

29. C. E. Baum, " The Magnetic Polarizability Dyadic and Point Symmetry," Interaction Note 502, May 1994. Air Force Weapons Lab.

30. P. Vafeas, G. Perrusson and D. Lesselier, "Low-frequency solution for a perfectly conducting sphere in a conductive medium with dipolar excitation," *Progress In Electromagnetics Research*, PIER 49, 87-111, 2004.

31. L. S. Riggs, J. E. mooney, D. E. Lawrence, J. T. Broach, and A. H. Trang, "On Identifying Conducting Objects using Low Frequency Magnetic Fields-Theory and Measurments," Interaction Note 542, July 1998. Air Force Weapons lab.

32. L. S. Riggs, J. E. Mooney, and D. E. Lawrence, "Identification of Metallic Mine-Like Objects Using Low Frequency Magnetic Fields", IEEE Transaction on GeoScience and Remote Sensing, Vol. 39, n1, Jan 2001, 56-66.

33. C. E. Baum, "Low-Frequency Near-Field Magnetic Scattering from Highly, but not perfectly, Conducting Bodies," Interaction Note 499, November, 1993. Air Force Weapons lab."

34. J. R. Wait, "A Conducting Sphere in a Time Varying Magnetic Field," *Geophysics*, Vol. 16, 666-672, 1951.

35. Y. Das, J. E. Mcfee, and R. Chesney, "Time Domain Response of a Sphere in the Field of a Coil: Theory and Experiments," *IEEE Transactions on Geosciences and Remote Sensing*, Vol. 22, no. 4, 360-367, July 1984.

36. J. R. Wait, . "A Conducting Permeable Sphere in the Presence of a Coil Carrying an Oscillating Current," Canadian Journal of Physics, Vol. 31, 670-678, 1953.

37. H. H. Braunisch, C. O. Ao, K. O'Neill and J. A. Kong, "Magnetoquasistatic response of conducting and permeable prolate spheroid under axial excitation," *IEEE Trans. Geoscience and Remote Sensing*, vol. 39, no. 12, 2689–2701, Dec. 2001.

38. Y. Das, J. E. Mcfee, and R. H. Chesney, "Determination of depth of shallowly buried objects by electromagnetic induction," *IEEE Trans. Geoscience and Remote Sensing*, Vol. 23, 60-66 , Jan 1985

39. S. J. Norton, and I. J. Won, "Identification of Buried Unexploded Ordnance from Broadband Electromagnetic Induction Data," *IEEE Trans. Geoscience and Remote Sensing*, Vol. 39, 2253-2261, Oct 2001

40. C. O. Ao, H. Braunisch, K. O'Neill and J. A. Kong, "Quasi-magnetostatic solution for a conducting and permeable spheroid with arbitrary excitation," *IEEE Trans. Geoscience and Remote Sensing*, vol. 40, no. 4, 887–897, Apr. 2002.

41. S.J. Norton, W.A. SanFilipo and I. J. Won, "Eddy-Current and Current-Channeling Response to Spheroidal Anomalies," *IEEE Trans. Geoscience and Remote Sensing*, Vol. 43, 2200-2209, Issue 10, Oct. 2005

42. G. D. Sower, "Eddy Current responses of Canonical Metallic Targets Theory and Measurements," Interaction Note 526, May 19, 1997, Air Force Weapons Lab.

43. S. K. Mukerji, M. George and M. B. Ramamurthy, "Eddy currents in solid rectangular cores," *Progress In Electromagnetics Research B* , PIER B, Vol. 7, 117-131, 2008

44. L.J. Bond, Clark, R. "Response of horizontal axis eddy current coils to layered media: a theoretical and experimental study*" IEE Proceedings A on Science, Measurement and Technology*, July 1991

45. M. Abramowitz, and I. A. Stegun, "Handbook of Mathematical Functions with Formulas, Graphs, and Mathematical Tables*",* New York: Dover, 1965

46. A. D. Kotsis, and J. A. Roumeliotis, "Electromagnetic scattering by a metallic spheroid using shape perturbation method," *Progress In Electromagnetics Research*, PIER 67, 113-134, 2007

47. M. D. Huang, and S. Y. Tan, "Efficient electrically small prolate spheroidal antennas coating with a shell of double-negative metamaterials ," *Progress In Electromagnetics Research*, PIER 82, 241-255, 2008

48. L. W. Li, and M. S. Leong "Spheroidal Coordinates and Wave Functions*" Spheroidal Wave Functions in Electromagnetic Theory*, November 2001.

49. R. F. Harrington, Time-Harmonic Electromagnetic Fields. McGraw-Hill,1961.

50. C. A. Balanis, Advanced Engineering Electromagnetics, Lohn Wiley & Sons, 1989

51. L. W. Li, and M. S. Leong "EM Scattering by a Conducting Spheroid*" Spheroidal Wave Functions in Electromagnetic Theory*, November 2001

Appendix A

In this part, there is a brief discussion only about the prolate spheroidal coordinates which is a spheroid generated by rotating an ellipse about its longer axis. You can consider a prolate spheroid centered at the origin with the z axis along its major axis. Assume the two foci are at $z = \pm D$ and the lengths of the semi major and semi minor axes are a and b, respectively with $(a > b)$. Then $D = \sqrt{a^2 - b^2}$ and the prolate spheroidal coordinates are expressed by [25]:

$$x = D\sqrt{\xi^2 - 1}\sin\vartheta\cos\phi \qquad \text{(A.1)}$$

$$y = D\sqrt{\xi^2 - 1}\sin\vartheta\sin\phi \qquad \text{(A.2)}$$

$$z = D\xi\cos\vartheta \qquad \text{(A.3)}$$

where $1 \le \xi < \infty$, $0 \le \vartheta \le \pi$, and $0 \le \phi \le 2\pi$. Evidently, ξ plays the role of the "radial" coordinate, ϑ is the spheroidal colatitudes angle, and ϕ is the azimuthal angle. The spheroidal coordinate ϑ is similar to the spherical colatitudes angle θ, and in the limit as $\xi \to \infty$ tends toward θ. You can consider that setting $\xi = \xi_0 = cons$ defines the surface of a spheroid; therefore the two parameters D and ξ_0 define its shape uniquely and are related to the parameters a and b by:

$$a = D\xi_0 \qquad b = D\sqrt{\xi_0^{\,2} - 1} \qquad \text{(A.4)}$$

In fact, the elasticity of the prolate spheroid is defined by $e = \sqrt{1 - b^2/a^2} = D/a = 1/\xi_0$, where $0 \le e \prec 1$. Thus, $e = 0$ implies a sphere and $e \to 1$, the spheroid stretches into a long thin rod. In the limit as the separation of the foci of the spheroid goes to zero $(D \to 0)$, the spheroid becomes a sphere and the prolate coordinates reduce to spherical ones. Clearly, as $D \to 0$, then $\xi \to \infty$ in such a way that $D\xi \to r$. Also in this limit, $D\xi_0 \to a$, where a is the radius of the limiting sphere, and $\vartheta \to \theta$.

And the same of other coordinates the gradient of the function $\psi(\xi, \vartheta, \phi)$ in spheroidal coordinates is given by:

$$\nabla \psi = \hat{\xi} \frac{1}{h_\xi} \frac{\partial \psi}{\partial \xi} + \hat{\vartheta} \frac{1}{h_\vartheta} \frac{\partial \psi}{\partial \vartheta} + \hat{\phi} \frac{1}{h_\phi} \frac{\partial \psi}{\partial \phi} \qquad \text{(A.5)}$$

where h shows metric scale factor. This scale factor changes for any of the unit vector such as mentioned below [25]:

$$h_\xi = D\frac{\sqrt{\xi^2 - \cos^2\vartheta}}{\sqrt{\xi^2 - 1}} \quad , \quad h_\vartheta = D\frac{\sqrt{\xi^2 - \cos^2\vartheta}}{\sin\vartheta} \quad \text{and} \quad h_\phi = D\sqrt{\xi^2 - 1}\sin\vartheta \qquad \text{(A.6)}$$

As $D \to 0$, one can show that $h_\xi \to D$, $h_\vartheta \to r$, $h_\phi \to r\sin\theta$, $\hat{\xi} \to \hat{r}$, and $\hat{\vartheta} \to \hat{\theta}$, as expected like the spherical coordinates. The main point should be considered here is that for the oblate

spheroidal coordinates the relations obtained by replacing D by jD, ξ by $j\xi$, and ξ_0 by $j\xi_0$, where now $D \equiv \sqrt{b^2 - a^2}$ and $\xi_0 = a/\sqrt{b^2 - a^2}$ [26].

Appendix B

Here it has listed a number of properties of Legendre functions. $P_1^0(\xi)$ and $P_1^1(\xi)$ are Legendre function of the first kind and $Q_1^0(\xi)$ and $Q_1^1(\xi)$ are Legendre functions of the second kind.

$$P_1^0(\xi)=\xi \tag{B.1}$$

$$P_1^1(\xi)=\sqrt{\xi^2-1} \tag{B.2}$$

The second kind Legendre functions, $Q_1^0(\xi)$ and $Q_1^1(\xi)$ can be expressed in terms of elementary functions as follows:

$$Q_1^0(\xi)=\frac{1}{2}\xi\ln\left(\frac{\xi+1}{\xi-1}\right)-1 \tag{B.3}$$

$$Q_1^1(\xi)=\sqrt{\xi^2-1}\left[\frac{\xi}{\xi^2-1}-\frac{1}{2}\ln\left(\frac{\xi+1}{\xi-1}\right)\right] \tag{B.4}$$

The derivatives of these functions with respect to ξ are

$$P_1^{0\prime}(\xi)=1 \tag{B.5}$$

$$P_1^{1\prime}(\xi)=\frac{\xi}{\sqrt{\xi^2-1}} \tag{B.6}$$

$$Q_1^{0\prime}(\xi)=\frac{1}{2}\ln\left(\frac{\xi+1}{\xi-1}\right)-\frac{\xi}{\xi^2-1} \tag{B.7}$$

$$Q_1^{1\prime}(\xi)=\frac{1}{\sqrt{\xi^2-1}}\left[1-\frac{1}{\xi^2-1}-\frac{1}{2}\xi\ln\left(\frac{\xi+1}{\xi-1}\right)\right] \tag{B.8}$$

Author's Publications

M. Mahmoudi and S. Y. Tan, "Depth detection of conducting marine mines via eddy-current and current-channeling response," *Progress In Electromagnetics Research*, PIER 90, 287-307, 2009.